Cross-stream migration of asymmetric particles driven by oscillating shear

2017 EPL 117 44001

(http://iopscience.iop.org/0295-5075/117/4/44001)

A Letters Journal Exploring the Frontiers of Physics

February 2017

EPL, **117** (2017) 44001
doi: 10.1209/0295-5075/117/44001

www.epljournal.org

Cross-stream migration of asymmetric particles driven by oscillating shear

M. Laumann[1], P. Bauknecht[2], S. Gekle[2], D. Kienle[1(a)] and W. Zimmermann[1]

[1] *Theoretische Physik I, Universität Bayreuth - 95440 Bayreuth, Germany*
[2] *Biofluid Simulation and Modeling, Universität Bayreuth - 95440 Bayreuth, Germany*

received 23 December 2016; accepted in final form 13 March 2017
published online 6 April 2017

PACS 47.15.G- – Low-Reynolds-number (creeping) flows
PACS 47.57.ef – Sedimentation and migration
PACS 83.50.-v – Deformation and flow

Abstract – We study the dynamics of asymmetric, deformable particles in oscillatory, linear shear flow. By simulating the motion of a dumbbell, a ring-polymer, and a capsule we show that cross-stream migration occurs for asymmetric elastic particles even in linear shear flow if the shear rate varies in time. The migration is generic as it does not depend on the particle dimension. Importantly, the migration velocity and migration direction are robust to variations of the initial particle orientation, making our proposed scheme suitable for sorting particles with asymmetric material properties.

Introduction. – During the recent years, microfluidics has evolved to a cross-disciplinary field, ranging from basic physics to a plethora of biological and technical applications [1–7], including the control of small amounts of fluids, chemical synthesis [8,9], biological analysis [10,11], and the study of the deformation dynamics of droplets, vesicles, capsules, or blood cells [12–40]. An important transport mechanism in microfluidic flows is the cross-stream migration (CSM), where particles move across streamlines and can be sorted due to their particle-specific properties [41,42].

The CSM effect has been first reported in 1961 by Segre and Silberberg for rigid particles at finite Reynolds number in pipes with diameters of several millimeters [43]. When channels approach the micrometer scale, the Reynolds number vanishes (Stokes regime) and fluid inertia does not matter; likewise, for μm-sized particles thermal effects can be discarded. In the Stokes regime, CSM arises in curvilinear [12–15] and rectilinear flow [16–20], if the particle is elastic and, in case of rectilinear flow, the flow's fore-aft symmetry is broken, requiring intra-particle hydrodynamic interaction [16–19]. Such symmetry breaking occurs near boundaries via wall-induced lift forces [19,21–23] or by space-dependent shear rates, so that dumbbells [16–18], droplets [24–26], vesicles and capsules [27–29] exhibit CSM even in unbounded flow. These parity breaking mechanisms may be accompanied by other effects due to viscosity contrast [24,44] or particle chirality [45], which further impact the CSM.

Here we show that a controlled cross-stream migration is possible even in unbounded *linear* shear flow, provided that 1) the particle holds an intrinsic asymmetry (parity breaking), and 2) the shear rate varies in time, causing time-dependent particle deformations. Importantly, the cross-stream migration occurs irrespective of the dimensionality of the particle, accentuating its *generic* nature, as we show by studying particles extending in one (1D), two (2D), and three (3D) dimensions. We demonstrate that the CSM depends on external flow parameters such as switching period, which can be controlled conveniently to achieve an optimized migration.

Model and approach. – To reveal the generic behavior of the CSM in oscillatory shear flow, we use three kinds of particles, which share the common features that they are deformable, asymmetric, and their constituent parts interact hydrodynamically. The first two particle types are a dumbbell (1D) and a ring-polymer (2D), modeled by a sequence of bead-spring units with the i-th bead located at $\mathbf{r}_i$ and connected to its nearest neighbors by linear springs

(a) E-mail: diego.kienle@uni-bayreuth.de (lead author and project coordination)

with an equilibrium bond length b and force constant k. The dumbbell asymmetry is modeled by assigning different friction coefficients ζ_1 and ζ_2 to unequal sized beads 1 and 2 with $r_\zeta = \zeta_2/\zeta_1 = 3$ (fig. 1(a), inset). The asymmetry of the N-bead ring-polymer is realized by a space-dependent bending stiffness $\kappa(\{\mathbf{r}\})$ along the ring contour $\{\mathbf{r}\}$. The third particle is an elastic capsule (3D), the asymmetry of which is implemented likewise by a spatially varying bending stiffness $\kappa(\{\mathbf{r}\})$ along the capsule surface $\{\mathbf{r}\}$. For the purpose of this study, we split the contour/surface of the ring/capsule in equal parts (Janus-particle); the stiff and bendy portion in either case has a bending stiffness of κ_2 and κ_1 with a ratio $r_\kappa = \kappa_2/\kappa_1 = 1.5$ (fig. 1(b) and (c), inset).

The migration behavior of all three particle kinds is obtained from their non-Brownian trajectories. The trajectories for the dumbbell and ring-polymer, exposed to an unperturbed flow field $\mathbf{u}(\mathbf{r})$, are determined by solving the standard Stokesian dynamics for bead-spring models [46],

$$\dot{\mathbf{r}}_i = \mathbf{u}(\mathbf{r}_i) + \sum_{j=1}^{N} \mathbf{H}_{ij} \cdot \left[\mathbf{F}_j^{bo} + \mathbf{F}_j^{be}\right]. \tag{1}$$

$\mathbf{F}_i^{bo}$ and $\mathbf{F}_i^{be}$ refer to harmonic bonding and bending forces, obtained from the potentials $U^{bo} = \sum_{i=1}^{N} \frac{k}{2}(R_i - b)^2$ and $U^{be} = -\sum_{i=1}^{N} \kappa(\mathbf{r}_i) \ln[1 + \cos\alpha_i]$. $R_i = |\mathbf{r}_i - \mathbf{r}_{i+1}|$ denotes the absolute value of the bond vector and $\cos\alpha_i = \mathbf{e}_{R_{i-1}} \cdot \mathbf{e}_{R_i}$ is the angle between the bond vectors $\mathbf{R}_{i-1}$ and $\mathbf{R}_i$ with $\mathbf{e}_{R_i} = \mathbf{R}_i/R_i$ the bond unit vector. The hydrodynamic interaction (HI) between bead i and j, inducing a hydrodynamic backflow (HB), is included in eq. (1) via the mobility matrix $\mathbf{H}_{ij}$ within the Oseen tensor [46],

$$\mathbf{H}_{ij} = \begin{cases} \frac{1}{8\pi\eta R_{ij}} \left[\mathbf{I} + \mathbf{e}_{R_{ij}} \otimes \mathbf{e}_{R_{ij}}\right] & i \neq j, \\ \frac{1}{\zeta_i}\mathbf{I} & i = j \end{cases} \tag{2}$$

with $\mathbf{e}_{R_{ij}} = \mathbf{R}_{ij}/R_{ij}$ and $\mathbf{R}_{ij} = \mathbf{r}_i - \mathbf{r}_j$. The capsule path is calculated using the immersed boundary method in conjunction with the lattice Boltzmann method for the flow [47–49], employing an adapted version of the ESPResSo package [50]. Throughout we assume a time-dependent (td), linear shear flow $\mathbf{u}(x, y) = S(t)y\,\mathbf{e}_x$ along the $\mathbf{e}_x$-axis; the shear rate $S(t)$ has a period T with $S(t) = +\dot{\gamma}$ during the first half-period T_1 and $S(t) = -\dot{\gamma}$ during the second half-period T_2 with $T_1 = T_2 = T/2$. The initial orientation of all three particles is $\phi_0 = 2.0\ \pi$ with the small ζ_1-bead, respectively, the stiff κ_2-contour/surface being located to the left.

Generic behavior. – Figure 1 shows the transverse component of the center of drag $y_c(t)$ (ζ-weighted), scaled with respect to the bond length b of the bead-spring unit or the capsule radius a, as a function of the scaled time $t\dot{\gamma}$ with fixed $\dot{\gamma}$ for all three particles. For symmetric particles ($r_{\zeta,\kappa} = 1.0$), the cross-stream migration is zero at any time (dashed line) [14,17] as parity breaking does not occur irrespective of whether the shear flow is stationary (ss) or time dependent (td). For asymmetric particles ($r_{\zeta,\kappa} > 1.0$) in *stationary* shear flow parity breaking exists, resulting indeed in a temporary CSM, as reflected in the oscillatory behavior of $y_c(t)$, whereas the *net* migration over one shear-cycle is still zero (red solid line). This interim migration of asymmetric particles can be exploited to attain a *net* cross-stream migration, if the shear rate $S(t)$ is made time dependent by switching $S(t)$ at a frequency $1/T$, as shown in fig. 1(a)–(c) by the blue solid

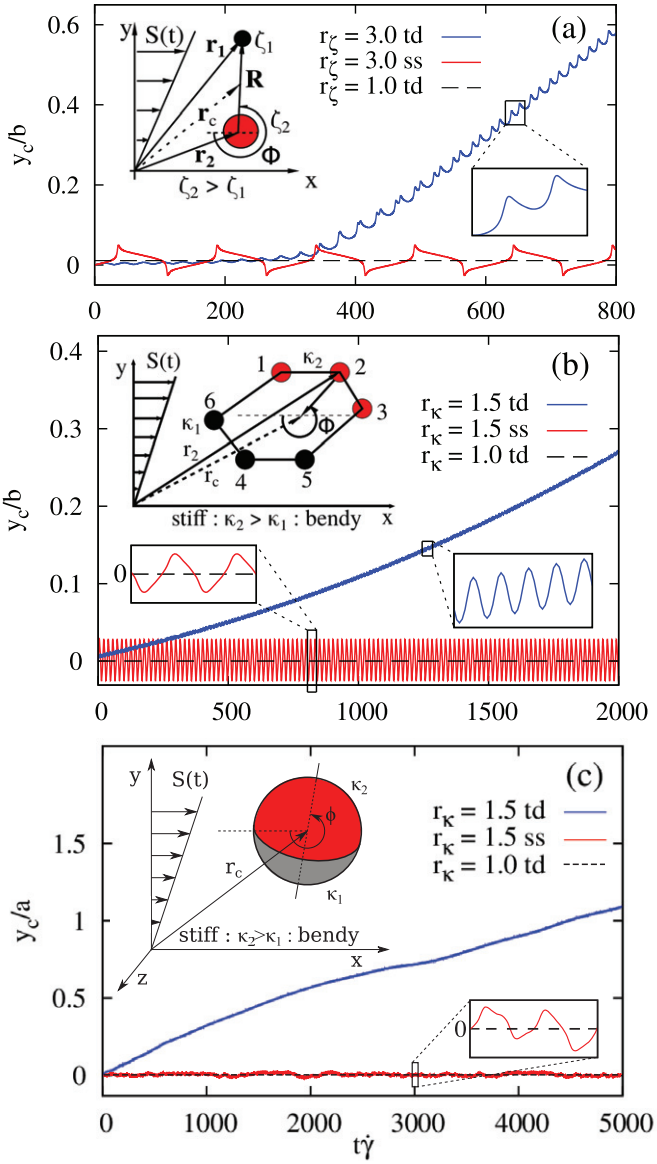

Fig. 1: (Color online) Lateral position $y_c(t)$ *vs.* scaled time $t\dot{\gamma}$ for the asymmetric (a) 1D dumbbell, (b) 2D ring, and (c) 3D capsule, sketches of which are shown in the inset. Irrespective of the model details, all particle types perform a *net* cross-stream migration in linear shear (blue solid), if the shear rate is time-dependent (td). At steady shear (ss), $y_c(t)$ oscillates around a constant mean (red solid), so that the *net* migration vanishes [14,17]. For symmetric particles ($r_{\zeta,\kappa} = 1.0$), the migration is zero. The initial orientation is $\phi_0 = 2.0\ \pi$.

line. The fact that all three particles display cross-stream behavior irrespective of their dimensionality and model details is an indication of a *generic* property[1], which can be attributed to the different *mean* shapes the particle acquires during each half-period, as discussed next.

Migration mechanism. – To understand the CSM mechanism, we take a closer look at the cross-stream dynamics of an asymmetric dumbbell ($r_\zeta > 1$) and an asymmetric ring ($r_\kappa > 1$), consisting of N-bead-spring units; we note that the discussion provided for the ring is general insofar as it applies for the 3D capsule as well where the ring is viewed as a 2D cut through the capsule plane of symmetry. To keep the explanation of the CSM mechanism transparent, we focus in either case on the *steady-state* regime (approached by all three particles after a transient), where the dumbbell and the ring have adopted a stable *mean* orientation $\langle\phi\rangle_{T/2}$ or $\langle\phi\rangle_T$, as determined by averaging their orientation angle $\phi(t)$ over a half or full shear-cycle, respectively.

Starting with the dumbbell, one can derive from eq. (1) a closed-analytical expression for the instantaneous cross-stream velocity $v_m(t)$ of its ζ-weighted center $y_c(t)$, as detailed in footnote [1] and given by

$$v_m(t) = \frac{k}{4\pi\eta}\,\frac{r_\zeta - 1}{r_\zeta + 1}\,\frac{R(t) - b}{R(t)}\,\sin\phi(t), \qquad (3)$$

with η the viscosity, $\phi(t)$ the orientation angle, and $R(t) = |\mathbf{r}_1 - \mathbf{r}_2|$ the distance between bead 1 and 2, as introduced in fig. 1(a). Equation (3) facilitates reading off various, well-known limiting cases: in linear shear flow CSM does not occur at any time ($v_m(t) = 0$), irrespective of whether the flow is stationary or time-dependent, if the dumbbell is i) symmetric ($r_\zeta = 1$), ii) very soft (small k), or iii) if HI is absent (free-draining) or weak, as realized for large bond lengths b [17].

Once the dumbbell is asymmetric ($r_\zeta > 1$) and simultaneously deformable (finite k), $v_m(t) \neq 0$, a *net* migration may be possible. Even though the precise conditions for a net migration step Δy_c during one half-cycle can be obtained only by integrating eq. (3), one can still gain important insights on the CSM mechanism by a qualitative inspection of eq. (3) and how the various terms interplay. First, as long as the switching period T and the shear rate $\dot\gamma$ are not too large to avoid full turnovers, the dumbbell orientation $\phi(t)$ oscillates (after a transient regime) around a mean angle $\langle\phi\rangle_{T/2} = 3\pi/2$ or $\pi/2$, depending on the initial orientation ϕ_0. When $\langle\phi\rangle_{T/2} = 3\pi/2$ ($\pi/2$), we observe that $\sin\phi(t)$ remains negative (positive) over the entire half-cycle and becomes largest once $\phi(t) \approx 3\pi/2$ ($\pi/2$), *i.e.*, the dumbbell is perpendicular to the flow direction, as shown in fig. 2(a). The bond length $R(t)$ oscillates also around the equilibrium bond length b, so that the term $R(t) - b$ in eq. (3) alters its sign (fig. 2(a)), causing the instantaneous CSM velocity $v_m(t) = \dot y_c(t)$ to oscillate (fig. 1(a)). Therefore, the sign of the *net* CSM depends on whether the positive or negative migration increments to Δy_c contribute most during the half-cycle.

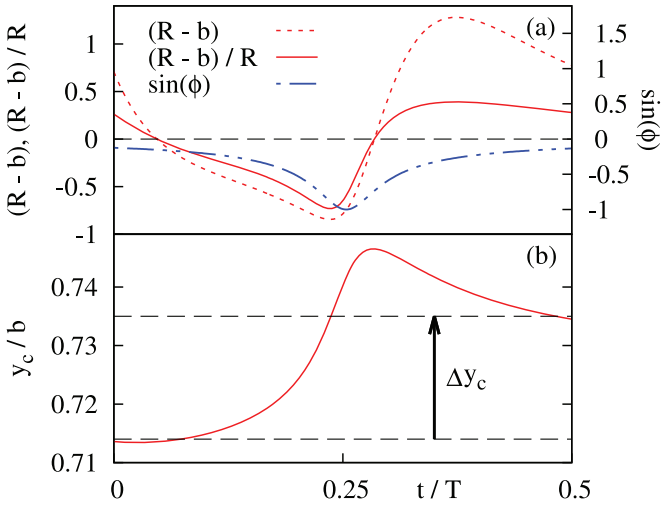

Fig. 2: (Color online) (a) Time dependence of the terms $R(t) - b$, $(R(t) - b)/R(t)$, and $\sin\phi(t)$, appearing in eq. (3), over a half period $T/2$ for the dumbbell orientation oscillating around $\langle\phi\rangle_{T/2} = 3\pi/2$. (b) Evolution of the transverse component of the center of drag $y_c(t)$, obtained by integrating eq. (3), and the *net* migration step $\Delta y_c > 0$ acquired at the end of $T/2$.

Based on eq. (3), one may expect that $\Delta y_c < 0$ because $\sin\phi(t) < 0$ over the whole half-cycle while the deformation $R(t) - b$ is asymmetric such that the dumbbell is stretched more strongly ($R(t) - b > 0$) than being compressed over $T/2$, as demonstrated in fig. 2(a) by plotting the respective terms of eq. (3); the asymmetry of $R(t) - b$ can be ascribed to the larger difference of the flow velocity between and hence larger drag on the beads when the dumbbell is stretched. However, a mean CSM with $\Delta y_c < 0$ is in clear contradiction to our numerical results, shown in fig. 1(a). The origin for the *net* migration step Δy_c being *positive* can be attributed to the non-linear behavior of the hydrodynamic interaction, appearing in eq. (3) via the $1/R(t)$-term, so that deformations of a compressed dumbbell receive a larger *negative* weight; fig. 2(a) displays the respective behavior of $(R(t) - b)/R(t)$, which is amplified furthermore by the peaking of $\sin\phi(t)$ when $R(t) - b < 0$. Hence, the positive contributions during the dumbbell compression outbalance the negative ones when the dumbbell is stretched. Our qualitative analysis, based on eq. (3), indicates that Δy_c is positive (negative) when the dumbbell swings around $\langle\phi\rangle_{T/2} = 3\pi/2$ ($\pi/2$). This qualitative picture is consistent with fig. 2(b), showing the evolution of $y_c(t)$ by integrating eq. (3) with the migration step $\Delta y_c > 0$ at the end of one half-cycle $T/2$, and is in full agreement with our numerical result shown

[1]The Supporting Information (SI) contains further details on the models, a derivation of eq. (4), plots and movies on the generic behavior (including an extension of the orientation robustness) of the dumbbell and capsule (`Movie1.mp4`, `Movie2.mp4`, `Movie3.mp4`, `Movie4.mp4`, `Movie5.mp4`, `Movie6.mp4`, `Movie7.mp4`, `Movie8.mp4`, `Movie9.mp4`, and `Supplementarymaterial.pdf`). A link of the abrupt v_m-drop to the $\langle\phi\rangle_T$-attractors is provided, too.

in fig. 1(a). Finally, we note that for a rigid dumbbell ($\dot{R}(t) = 0$) the migration step $\Delta y_c = 0$ when swinging around $\langle\phi\rangle_{T/2} = 3\pi/2$ ($\pi/2$), as one can show by solving eq. (3) analytically (see footnote [1]).

We now inspect the CSM behavior of the 2D ring and assume again that both the period T and the shear rate $\dot{\gamma}$ are not too large as to prevent the ring dynamics being dominated by tank-treading, causing a net zero migration, as discussed in the following paragraphs. Under this condition and for an initial orientation ϕ_0, the ring adopts (after a transient) one stable *mean* orientation $\langle\phi\rangle_T$ over one shear-cycle T. Specifically, for $\phi_0 = 2.0\ \pi$ the mean orientation of the ring is $\langle\phi\rangle_T \approx 1.75\ \pi$ with the stiff contour located in the upper (left) half-space and referred to below. We note that other initial orientations ϕ_0 may lead to one of the other possible mean orientations with $\langle\phi\rangle_T \approx 1.25\ \pi$, $\approx 0.75\ \pi$, or $\approx 0.25\ \pi$, where the ring (and capsule) displays CSM. Importantly, the explanation of the CSM mechanism provided for the mean orientation $\langle\phi\rangle_T \approx 1.75\ \pi$ and shown in fig. 1(b) applies irrespective of the specific value of $\langle\phi\rangle_T$.

Since a closed semi-analytic expression of the CSM velocity similar to eq. (3) is not possible beyond dumbbell models, we analyze the migration of the ring in terms of the *mean steady-state* CSM velocity $v_m^i = \langle v_m(\infty)\rangle_{T_i}$ (along the y-axis) for each half-period T_i, obtained by averaging the velocity $v_m(t)$ over T_i (see footnote [1]),

$$v_m^i = \langle \mathbf{e}_y \cdot \dot{\mathbf{r}}_c(\infty)\rangle_{T_i} = \frac{1}{N}\sum_{i=1}^{N}\sum_{j\neq i}\langle \mathbf{e}_y \cdot \mathbf{H}_{i,j} \cdot \mathbf{F}_j\rangle_{T_i}. \quad (4)$$

Equation (4) implies that for rectilinear flows with $\mathbf{e}_y \cdot \mathbf{u} = 0$, the cross-stream transport is entirely driven by the particle drag due to the hydrodynamic backflow, induced by the potential forces $\mathbf{F}_j$. Further, the magnitude and direction of each HB (and hence of v_m^i) depend on the particle shape via the force profile $\mathbf{F}(\{\mathbf{r}_j\})$ and the dyadic mobility matrix $\mathbf{H}_{i,j}$. An expression similar to eq. (4) can be used to determine the *mean* HI-induced flow field $\mathbf{v}(\mathbf{r})$ for each half-period (see footnote [1]). The respective 2D backflow $\mathbf{v}(\mathbf{r})$, shown in fig. 3(a) and (b) when $\langle\phi\rangle_T \approx 1.75\ \pi$, corresponds to an *elongational* flow, whose flow lines are reversed (sign change) as a result of the altering ring deformation during the $S(t)$-switching ($+\dot{\gamma} \to -\dot{\gamma}$), and displayed more clearly in fig. 3(c) and (d). The ring asymmetry causes generally a break of the parity symmetry (PS) of the elongational HB, but the extent of the PS violation depends on the strength of the *mean* deformation during each half-cycle T_i (fig. 3(c) and (d)).

Comparing the *mean* deformation for each half-cycle, one observes that the ring asymmetry is *enhanced* during the first T_1 shear-cycle, causing an increased parity break of the elongational HB (fig. 3(c)). But this implies that the *difference* between the mean opposing partial HB-drags at the stiff and bendy side, v_m^s and v_m^b (see footnote [1]: eq. (9) of the SI), becomes larger with $|v_m^s| > |v_m^b|$ since $\kappa_2 > \kappa_1$.

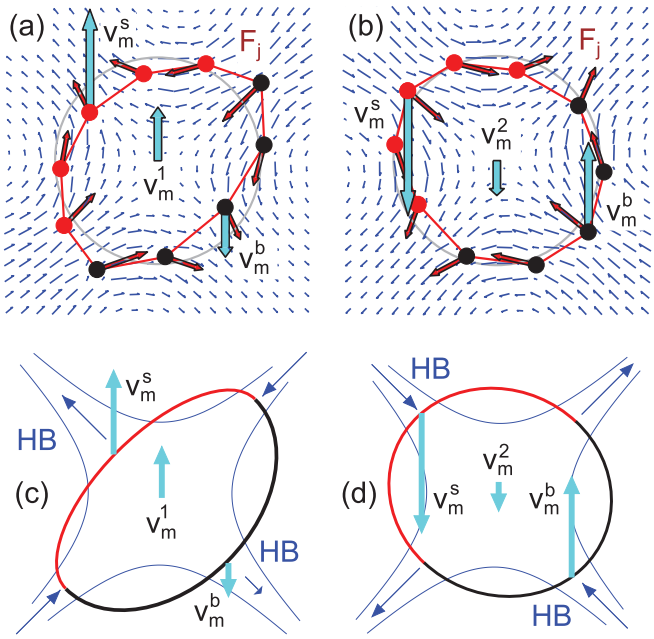

Fig. 3: (Color online) Explanation of the basic migration mechanism by way of the ring. Shown are simulation data for the *mean* ring shape, averaged over the (a) first T_1 and (b) second T_2 shear-cycle, and the potential forces $\mathbf{F}_j$ along the N-bead contour. While the backflow $\mathbf{v}(\mathbf{r})$ (HB) induced within each half-cycle T_i is approximately elongational (blue), its parity is broken due to the particle asymmetry and leads to different mean CSM-driving drags v_m^s and v_m^b at the stiff and bendy side. Panels (c) and (d) show how the parity asymmetry of the HB is enhanced ($|v_m^s| > |v_m^b|$) during the T_1-cycle, while during the T_2-cyle the HB-parity is partially recovered ($|v_m^s| \gtrsim |v_m^b|$), leading to a *net* positive migration $v_m = v_m^1 + v_m^2 > 0$.

Hence, the *mean* migration velocity during the T_1-cycle, $v_m^1 = v_m^s + v_m^b$, is large and *positive*. In turn, during the T_2 shear-cycle the situation is reversed as the ring shape is roughly circular, *i.e.*, the ring asymmetry is *reduced* with the result that the parity of the elongational backflow is partly recovered (fig. 3(b) and (d)), and the opposing partial HBs almost cancel. The reason for the residual backflow is because the HB-drag at the stiff contour part is slightly larger than at the bendy side ($|v_m^s| \gtrsim |v_m^b|$), as a result of the larger stiffness. During the T_2-cycle the *mean* migration step $v_m^2 = v_m^s + v_m^b$ is thus small and *negative*. Over the course of one shear-cycle $T = T_1 + T_2$, the *net* migration $v_m = v_m^1 + v_m^2$ is therefore *positive*, as displayed by all three kinds of particles (fig. 1(a)–(c)).

Orientation robustness. – We now demonstrate that the CSM effect is quite robust against a dispersal of initial orientations by varying the angle ϕ_0, while keeping the orientation axis within the y-x shear plane (tilt angle $\theta_0 = 0$). Figure 4 shows the instantaneous migration velocity of the ring $\langle v_m(t)\rangle_T \tau_b/b$, averaged over one cycle T, *vs.* time $t\dot{\gamma}$ ($\dot{\gamma} = 0.1$ fixed, $\tau_b = \eta b^3/\kappa_1$) for various orientations ϕ_0 within the intervals $I^+ = [1.1; 2.0]\pi$ and $I^- = [0.1; 1.0]\pi$. The interval I^+ (I^-) corresponds to ring

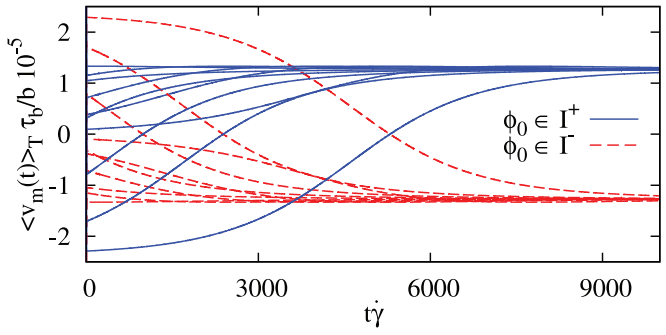

Fig. 4: (Color online) Instantaneous migration velocity $\langle v_m(t)\rangle_T \tau_b/b$ of the ring, averaged over one period T, *vs.* time $t\dot\gamma$ for different initial angles ϕ_0 taken out of the interval $I^+ = [1.1; 2.0]\,\pi$ or $I^- = [0.1; 1.0]\,\pi$. The $\langle v_m(t)\rangle_T$-transient depends on ϕ_0, while the steady-state value $v_m = \langle v_m(\infty)\rangle_T$ is ϕ_0-independent. Parameters: $\dot\gamma = 0.1$, $T = 20$, $r_\kappa = 1.5$.

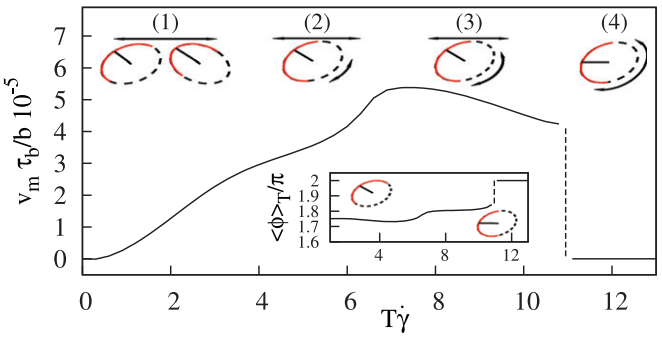

Fig. 5: (Color online) Steady-state migration velocity $v_m\tau_b/b$ of the ring *vs.* switching period $T\dot\gamma$. Four dynamic regimes are identified: (1) oscillatory shear deformation, indicated by the horizontal arrow, at small T; (2) weak tank-treading (TT) superposed with (1), marked by the half-circle arrow; (3) enhanced tank-treading at large T; (4) TT-dominated with zero net migration for $T\dot\gamma > 11$. Inset: T-averaged mean orientation $\langle\phi\rangle_T$ *vs.* $T\dot\gamma$. Parameters: $\phi_0 = 2.0\ \pi$, $\dot\gamma = 0.1$, $r_\kappa = 1.5$.

orientations, where during migration the stiff part lies in the mean within the upper (lower) half-space with the orientation angle $\phi(t)$ oscillating either around the *mean* $\langle\phi\rangle_T \approx 1.75\ \pi$ or $1.25\ \pi$ ($\langle\phi\rangle_T \approx 0.75\ \pi$ or $0.25\ \pi$). As discussed before, this implies that the final, steady-state migration velocity $v_m \equiv \langle v_m(\infty)\rangle_T$, is positive for $\phi_0 \in I^+$ and negative for $\phi_0 \in I^-$, as disclosed in fig. 4 for $t\dot\gamma > 9.0 \cdot 10^3$. Remarkably, the ring migrates always at the same steady-state speed $v_m^{+/-}$ even though the ϕ_0-orientation varies by almost $\Delta\phi_0^{+/-} \approx \pi$, meaning $v_m^{+/-}$ is independent of ϕ_0. In turn, the choice of ϕ_0 determines strongly the short-time dynamics of $\langle v_m(t)\rangle_T$, as shown in fig. 4 for $t\dot\gamma < 9.0 \cdot 10^3$. This imbalance of the magnitude and in part the sign of $\langle v_m(t)\rangle_T$ is a transient signature and exists as the orientation angle $\phi(t)$ is not yet in-phase with the shear signal $S(t)$; the phase synchronization of the angle takes place gradually within the transient regime over many shear-cycles T before a phase-locking is established. The behavior of $\langle v_m(t)\rangle_T$, shown for the ring in fig. 4, is generic and displayed by the other particles types (see footnote [1]).

We note that while the migration persists ($v_m \neq 0$) in most cases when the tilt angle θ_0 between the particle axis and the y-x shear plane is non-zero (accentuating the robustness of the CSM effect), some signatures of the migration alter when $\theta_0 \neq 0$ and depend on the particle type, which we briefly summarize below with more details provided in the SI (see footnote [1]). In case of the dumbbell, the tilt angle $\theta(t)$ always relaxes back towards the y-x shear plane ($\theta(\infty) = 0$) for any value of $\theta_0 \in [0.0; \pi/2[$, so that $\langle\theta\rangle_T^{FP} = 0$ is an asymptotically stable fixed point; only for one tilt angle $\theta_0 = \pi/2$, the dumbbell retains its initial orientation within the z-x plane, in which case $\langle\theta\rangle_T^{FP} = \frac{\pi}{2}$ is a *neutral stable* fixed point and corresponds to a non-migrating state ($v_m = 0$). The dumbbell migration is, therefore, robust against θ_0-variations over the entire interval $\pi/2$. The capsule behaves likewise and exhibits orientational relaxation as well, except that the previous robustness interval for θ_0 is reduced to $[0; \frac{2}{3}]\frac{\pi}{2}$ with $v_m \neq 0$, while the residual interval $]\frac{2}{3}; 1.0]\frac{\pi}{2}$ leads to zero migration, as the capsule axis relaxes to the other stable fixed point $\langle\theta\rangle_T^{FP} = \frac{\pi}{2}$. The ring migration differs from the dumbbell and capsule insofar as *all* tilt angles θ_0 are *neutral stable* fixed points, *i.e.*, $\langle\theta\rangle_T^{FP} = \theta_0 \in [0; \frac{\pi}{2}]$, implying that the ring keeps its initial θ_0-orientation. The non-relaxation of the tilt angle has the consequence that the ring moves at a different (but constant) speed for each value $\theta_0 \in [0; \frac{\pi}{2}[$. Again, the CSM of the ring is robust over the entire θ_0-interval of $\pi/2$.

Frequency dependence. – The migration process is not entirely determined by the material properties of the particle (*e.g.*, stiffness), but can be controlled also by external parameters such as the shear rate $\dot\gamma$ or the switching period T, the latter being discussed next. Figure 5 shows the steady-state migration velocity $v_m\tau_b/b$ for a fixed $\dot\gamma = 0.1$ *vs.* the period $T\dot\gamma$, which sets the time scale for the sign change of the shear rate $S(t)$. When $T\dot\gamma$ is small, the migration speed v_m is rather low (regime (1)) since the quickly alternating shear rate $S(t)$ induces only a small shear deformation of the ring shape, so that the ring has not sufficient time to reorient and to fully develop its mean conformation within each half-period T_1 and T_2, respectively; at these short times tank-treading is still marginal, as sketched in fig. 5. For larger periods T, the ring has now more time within each half-cycle to deform and fully adopt the migration state, so that v_m monotonously grows first (regime (2)), approaching a maximum at $T\dot\gamma \approx 7$. At this stage, a weak partial tank-treading (TT) of the contour is initiated, but the ring dynamics is still dominated by oscillatory shear deformations, driving the CSM. Beyond a value of $T\dot\gamma > 7$ the migration gradually decays since tank-treading becomes increasingly important insofar as a larger fraction of time of each half-cycle T_i is spent on tank-treading.

This implies that a portion of the stiff/bendy contour is now partly shuffled from the upper/lower half-space to the lower/upper one (regime (3)), *i.e.*, the dynamics of the entire shear-cycle takes now place within two half-spaces (with an unequal amount) and each contributes to the CSM with opposite sign. The *net* velocity v_m is still positive, since the *mean* orientation of the ring $\langle\phi\rangle_T \approx 1.75\pi$ (fig. 5, inset) with the stiff/bendy contour part residing on *average* within the upper/lower half-space. Beyond $T\dot{\gamma} > 11$ the CSM comes to a halt since tank-treading dominates now the dynamics within each half-period, so that even a larger fraction of the stiff/bendy contour is reshuffled between the upper-lower half-space. Within this TT-dominated regime, the *mean* orientation flips from $\langle\phi\rangle_T \approx 1.75\ \pi$ ($v_m > 0$) to $\langle\phi\rangle_T \approx 2.0\ \pi$ (fig. 5, inset), which corresponds to a *symmetric* state where equal amounts of the stiff/bendy contour lie in the *mean* within both half-spaces, so that v_m is zero (see footnote [1]). The abrupt v_m-drop is hence inherently connected with the abrupt change of the *mean* orientation $\langle\phi\rangle_T$, which can be understood by inspecting the phase-space $\langle\dot{\phi}(t)\rangle_T$-$\langle\phi(t)\rangle_T$ (see SI in footnote [1] for details). Here we just note that the phase-space features a pattern of discrete, *asymptotically stable* orientations $\langle\phi\rangle_T^{FP}$ (fixed points), which the ring can access. Importantly, the number and value of available $\langle\phi\rangle_T^{FP}$ depend sensitively on the switching period T (see footnote [1]). In our case with $\phi_0 = 2.0\ \pi$, the only stable orientation the ring can adopt is $\langle\phi\rangle_T^{FP} \approx 1.75\ \pi$ as long as $T\dot{\gamma} < 11$ while $\langle\phi\rangle_T \approx 2.0\ \pi$ is unstable[2]. When $T\dot{\gamma} > 11$, the previous fixed point at $1.75\ \pi$ disappears, so that the orientation $\langle\phi(t)\rangle_T \approx 1.75\ \pi$ is acquired only temporarily while a new orientational attractor appears at $\langle\phi\rangle_T^{FP} = 2.0\ \pi$. Since the value $1.75\ \pi$ lies within the (extended) range of the 2π-attractor, the ring locks in to the mean orientation of $\langle\phi\rangle_T = 2.0\ \pi$ (fig. 5, inset), corresponding to a non-migrating state ($v_m = 0$) (see footnote [1]).

Conclusions. – We have shown that deformable particles, which hold an intrinsic asymmetry (parity breaking), display cross-stream migration (CSM) in time-perodic, linear shear flow for medium switching frequencies. The net migration can be attributed uniquely to the particle asymmetry as it leads to an asymmetric force distribution within the periodically deformed particle, inducing asymmetric, non-compensating hydrodynamic backflows (HBs). Since the magnitude and direction of the HBs depend on the actual particle deformation, which is different within the first and second half-period, the HBs averaged over one shear-cycle T are non-zero, thus leading to a finite CSM (fig. 3). The CSM is *generic* inasmuch as it does not depend on the particle dimension nor on the specific details of its asymmetry (fig. 1(a)–(c)). While the migration direction is sensitive to whether the stiff/bendy part of the particle resides during one shear cycle in the mean within the upper or lower half-space, the CSM speed approaches after a transient phase a constant value and is independent of the initial particle orientation (fig. 4).

Given that even a small asymmetry in the bending modulus (factor 1.5 or less) of micron-sized particles can trigger for medium channel lengths a sizable migration velocity of 20 $\frac{\mu\mathrm{m}}{\mathrm{min}}$ under realistic flow conditions with a shear rate of $\dot{\gamma} = 22\ \frac{1}{\mathrm{s}}$ and a period of $T = 1.75\,\mathrm{Hz}$ (see footnote [1]), our proposed scheme facilitates appreciable migration distances in compact microfluidic setups just by independently tuning the amplitude and frequency of the shear rate. Investigating effects due to random material inhomogeneities will be an interesting subject for future studies.

* * *

PB and SG thank the Volkswagen foundation for support and gratefully acknowledge the Leibniz Supercomputing Center Munich for the provision of computing time. ML and WZ acknowledge support by the DFG priority program on Micro- and Nanofluidics.

REFERENCES

[1] Squires T. M. and Quake S. R., *Rev. Mod. Phys.*, **77** (2005) 978.
[2] Whitesides G. M., *Nature*, **442** (2006) 368.
[3] Popel A. S. and Johnson P. C., *Annu. Rev. Fluid Mech.*, **37** (2005) 43.
[4] Graham M. D., *Annu. Rev. Fluid Mech.*, **43** (2011) 273.
[5] Dahl J. B., Lin J.-M. G., Muller S. J. and Kumar S., *Ann. Rev. Chem. Biomol. Eng.*, **6** (2015) 293.
[6] Sackmann E. K., Fulton A. L. and Beebe D. L., *Nature*, **507** (2014) 181.
[7] Amini H., Lee W. and Di Carlo D., *Lab Chip*, **14** (2014) 2739.
[8] Jähnisch K., Hessel V., Löwe H. and Baerns M., *Angew. Chem., Int. Ed.*, **43** (2004) 406.
[9] Elvira K. S., Casadevall i Solvas X., Wootton R. C. R. and deMello A. J., *Nat. Chem.*, **5** (2013) 905.
[10] Yi C., Li C.-W., Ji S. and Yang M., *Anal. Chim. Acta*, **560** (2006) 1.
[11] Chen J., Li J. and Sun Y., *Lab Chip*, **12** (2012) 1753.
[12] Shafer R. H., Laiken N. and Zimm B. H., *Biophys. Chem.*, **2** (1974) 180; Shafer R. H., *Biophys. Chem.*, **2** (1974) 185.
[13] Aubert J. H. and Tirrell M., *J. Chem. Phys.*, **72** (1980) 2694; Aubert J. H., Prager S. and Tirrell M., *J. Chem. Phys.*, **73** (1980) 4103.
[14] Nitsche L. C., *AIChE J.*, **42** (1996) 613.
[15] Ghigliotti G., Rahimian A., Diros G. and Misbah C., *Phys. Rev. Lett.*, **106** (2011) 028101.
[16] Sekhon G., Armstrong R. C. and Jhon M. S., *J. Polym. Sci.*, **20** (1982) 947.
[17] Brunn P. O., *Int. J. Multiphase Flow*, **9** (1983) 187.

[2]We note that whether the system approaches an attractive fixed point does also depend on the *range* of each attractor. In the case of the ring, the 2π-fixed point is unstable for $T\dot{\gamma} = 9.0$, but turns into a stable FP when $T\dot{\gamma} = 10.0$. Since the range of the 2π attractor is quite small, the ring does not approach this FP, but continues to lock in to the orientational attractor $\langle\phi\rangle_T^{FP} \approx 1.8\ \pi$ due to its larger range. More details are provided in the SI (see footnote [1]).

[18] Brunn P. O. and Chi S., *Rheol. Acta*, **23** (1984) 163.
[19] Jhon M. S. and Freed K. F., *J. Polym. Sci.*, **23** (1985) 955.
[20] Agarwal U. S., Datta A. and Mashelkar R. A., *Chem. Eng. Sci.*, **49** (1994) 1693.
[21] Cantat I. and Misbah C., *Phys. Rev. Lett.*, **83** (1999) 880.
[22] Seifert U., *Phys. Rev. Lett.*, **83** (1999) 876.
[23] Ma H. B. and Graham M. D., *Phys. Fluids*, **17** (2005) 083103.
[24] Haber S. and Hetsroni G., *J. Fluid Mech.*, **49** (1971) 257.
[25] Leal L. G., *Annu. Rev. Fuid Mech.*, **12** (1980) 435.
[26] Mandal S., Bandopadhyay A. and Chakraborty S., *Phys. Rev. E*, **92** (2015) 023002.
[27] Kaoui B., Ristow G. H., Cantat I., Misbah C. and Zimmermann W., *Phys. Rev. E*, **77** (2008) 021903.
[28] Danker G., Vlahovska P. M. and Misbah C., *Phys. Rev. Lett.*, **102** (2009) 148102.
[29] Doddi S. K. and Bagchi P., *Int. J. Multiphase Flow*, **34** (2008) 966.
[30] Sibillo V., Pasquariello G., Simeone M., Cristini V. and Guido S., *Phys. Rev. Lett.*, **97** (2006) 054502.
[31] Abkarian M. and Viallat A., *Soft Matter*, **4** (2008) 653.
[32] Dupire J., Abkarian M. and Viallat A., *Phys. Rev. Lett.*, **104** (2010) 168101.
[33] Baroud C. N., Gallaire F. and Dangla R., *Lab Chip*, **10** (2010) 2032.
[34] Deschamps J., Kantsler V., Segre E. and Steinberg V., *Proc. Natl. Acad. Sci. U.S.A.*, **106** (2009) 11444.
[35] Kessler S., Finken R. and Seifert U., *Eur. Phys. J. E*, **29** (2009) 399.
[36] Noguchi H., *Phys. Rev. E*, **81** (2010) 061920.
[37] Zhao M. and Bagchi P., *Phys. Fluids*, **23** (2011) 111901.
[38] Matsunaga D., Imai Y., Yamaguchi T. and Ishikawa T., *J. Fluid Mech.*, **762** (2015) 288.
[39] Zhu L., Rabault J. and Brandt L., *Phys. Fluids*, **27** (2015) 071902.
[40] Cordasco D. and Bagchi P., *J. Fluid Mech.*, **800** (2016) 484.
[41] Sajeesh P. and Sen A. K., *Microfluid. Nanofluid.*, **17** (2014) 1.
[42] Geislinger T. M. and Franke T., *Adv. Colloid Interface Sci.*, **208** (2014) 161.
[43] Segre G. and Silberberg A., *Nature*, **189** (1961) 209.
[44] Farutin A. and Misbah C., *Phys. Rev. Lett.*, **109** (2012) 248106.
[45] Watari N. and Larson R. G., *Phys. Rev. Lett.*, **102** (2009) 246001.
[46] Doi M. and Edwards S. F., *The Theory of Polymer Dynamics* (Oxford University Press, Oxford) 1986.
[47] Krüger T., Varnik F. and Raabe D., *Comput. Math. Appl.*, **61** (2011) 3485.
[48] Guckenberger A., Schraml M. P., Chen P. G., Leonetti M. and Gekle S., *Comput. Phys. Commun.*, **207** (2016) 1.
[49] Bächer C., Schrack L. and Gekle S., *Phys. Rev. Fluids*, **2** (2017) 013102.
[50] Arnold A. *et al.*, *ESPResSo 3.1 - Molecular Dynamics Software for Coarse-grained Models* (Springer, Berlin) 2013.

Cross-stream migration of asymmetric particles driven by oscillating shear

– Supporting Information –

(Dated: March 13, 2017)

The supplementary note provides further details on the models and parameters used to simulate the cross-stream migration (CSM) of the dumbbell (1D), ring-polymer (2D), and capsule (3D) in linear shear flow. The *generic* behavior of the CSM is demonstrated further by complementing the simulations of the ring (shown in Fig. 4 and 5 in the main text) with corresponding plots, cf. Figs. 1 and 2 for the dumbbell and capsule, respectively.

I. DETAILS ON MODELS AND APPROACH

A. Bead-Spring: Dumbbell (1D) and Ring-Polymer (2D)

The dumbbell and the ring polymer are represented by a string of N beads, which over-damped dynamics for each bead i at position $\mathbf{r}_i$ is given by

$$\dot{\mathbf{r}}_i = \mathbf{u}(\mathbf{r}_i) + \sum_{j=1}^{N} \mathbf{H}_{ij} \cdot \left[\mathbf{F}_j^{bo} + \mathbf{F}_j^{be}\right] \tag{1}$$

with $\mathbf{F}_i^{bo} = -\nabla_{\mathbf{r}_i} U^{bo}$ and $\mathbf{F}_i^{be} = -\nabla_{\mathbf{r}_i} U^{be}$ referring to the harmonic bonding and bending forces, obtained from the respective potential

$$U^{bo} = \sum_{i=1}^{N} \frac{k}{2} \left(R_i - b\right)^2 \ , \qquad U^{be} = -\sum_{i=1}^{N} \kappa\left(\mathbf{r}_i\right) \ln\left[1 + \cos\alpha_i\right] \ . \tag{2}$$

The parameters k, b, and R_i denote the force constant, equilibrium bond length, and absolute value of the bond vector $R_i = |\mathbf{R}_i| = |\mathbf{r}_i - \mathbf{r}_{i+1}|$, respectively; $\kappa\left(\mathbf{r}\right)$ refers to the space-dependent bending stiffness and $\cos\alpha_i = \mathbf{e}_{R_{i-1}} \cdot \mathbf{e}_{R_i}$ is the angle between the bond vectors $\mathbf{R}_{i-1}$ and $\mathbf{R}_i$ with $\mathbf{e}_{R_i} = \mathbf{R}_i / R_i$ the bond unit vector.

The mobility matrix $\mathbf{H}_{ij}$ accounts for the hydrodynamic interaction (HI) between bead i and j, which in the Oseen-approximation[1] reads

$$\mathbf{H}_{ij} = \begin{cases} \frac{1}{8\pi\eta R_{ij}} \left[\mathbf{I} + \mathbf{e}_{R_{ij}} \otimes \mathbf{e}_{R_{ij}}\right] & : i \neq j \\ \frac{1}{\zeta_i}\mathbf{I} & : i = j \end{cases} \tag{3}$$

where $\mathbf{e}_{R_{ij}} = \mathbf{R}_{ij}/R_{ij}$ with $\mathbf{R}_{ij} = \mathbf{r}_i - \mathbf{r}_j$, and $\zeta_i = 6\pi\eta a_i$ the Stokes drag coefficient for a single bead with radius a_i.

The unperturbed flow field $\mathbf{u}(\mathbf{r})$ in Eq. (1) is given by the linear shear along the x-axis

$$\mathbf{u}(x, y) = S(t) y \, \mathbf{e}_x \tag{4}$$

with a time-dependent shear rate $S(t)$.

If the dumbbell is exposed to the linear shear flow $\mathbf{u}(x, y)$ only, it will not continuously perform a tumbling and rotational motion, rather rotates as to align with the streamlines along the x-axis. This behavior is known to be unphysical and a consequence of approximating the hydrodynamic interaction to first order only via the Oseen-tensor, assuming point-like particles. In general, this restriction could be lifted by including third-order corrections to the HI and thus reproduce the tumbling/rotational motion for the dumbbell[2]. Instead, we amend the linear shear flow $\mathbf{u}(x, y)$ by the flow-field[3]

$$\mathbf{v}^{\mathrm{rot}}(\mathbf{r}_i) = \frac{1}{2} \left(\frac{a_j}{R_{ji}} \right)^3 (\mathbf{r}_j - \mathbf{r}_i) \times [\nabla \times \mathbf{u}(\mathbf{r}_j)] \ , \tag{5}$$

which accounts for the rotation of finite-sized, spherical beads when being exposed to the shear flow of Eq. (4). In this manner, we capture the correct physics of the torque-induced tumbling and rotation of the dumbbell in the presence of flows with shear gradients.

The inclusion of tumbling and rotation in the dumbbell dynamics, as mediated by $\mathbf{v}^{\mathrm{rot}}(\mathbf{r})$, ensures that the dumbbell can develop a transient dynamics (main text: Fig. 1 (a)), where its orientation $\phi(t)$ is not yet in phase with the external shear signal $S(t)$; the presence of such a transient regime, however, is critical for establishing a phase synchronization of $\phi(t)$ (phase-locking), so that the dumbbell approaches ultimately a mean steady state orientation. Importantly, once the phase is locked the flow-field $\mathbf{v}^{\mathrm{rot}}(\mathbf{r})$ is no longer critical to describe the dumbbell dynamics at steady state. Yet, launching the dumbbell using just Eq. (1) without the $\mathbf{v}^{\mathrm{rot}}(\mathbf{r})$ term would not reproduce the correct transient dynamics, required to reach phase-locking and a mean orientation. We note that in case of the 2D ring and 3D capsule the tumbling and rotation dynamics is naturally captured by their dynamic equation, because both particles are already extended objects, so that the flow field $\mathbf{v}^{\mathrm{rot}}(\mathbf{r})$ does not need to be included in their dynamic equations.

Table I lists the parameters for the two bead-spring particles (bond length b, bead radii a_i, force constant k, bending stiffness $\kappa_{1,2}$), and the shear flow (shear rate $\dot{\gamma}$, period T,

viscosity η) used in the simulation of the 1D dumbbell and the 2D ring-polymer. With these parameters a timescale for the relaxation of the dumbbell and ring can be defined via $\tau = \zeta_1/k$ and $\tau_b = \eta b^3/\kappa_1$, respectively.

TABLE I: Dimensionless parameters used in the simulation of the 1D dumbbell and 2D ring.

particle kind	b	a_i	k	$\kappa_{1,2}$	$\dot{\gamma}$	T	η
dumbbell	2.0	0.1/0.3	1.0	N/A	1.0	30.0	1.0
ring-polymer	2.0	0.3	1.0	16.0/24.0	0.1	20.0	1.0

B. Bead-Spring: General Expression for Migration Velocity

An expression for the *instantaneous* velocity of cross-stream migration $v_m(t)$ can be derived by introducing the ζ-weighted center of drag $\mathbf{r}_c(t) := 1/\tilde{\zeta}\sum_{i=1}^{N}\zeta_i\ \mathbf{r}_i(t)$ for N beads with $\tilde{\zeta} = \sum_{i=1}^{N}\zeta_i$ the total drag coefficient. The velocity of the drag center follows then directly from $\dot{\mathbf{r}}_c(t)$; using Eq. (1) for $\dot{\mathbf{r}}_i(t)$ and taking into account that the sum of the total potential forces $\sum_{i=1}^{N}\mathbf{F}_i = 0$ with $\mathbf{F}_i = \mathbf{F}_i^{bo} + \mathbf{F}_i^{be}$, one obtains

$$\dot{\mathbf{r}}_c(t) = \frac{1}{\tilde{\zeta}}\sum_{i=1}^{N}\zeta_i\left[\mathbf{u}(\mathbf{r}_i) + \sum_{j\neq i}\mathbf{H}_{i,j}\cdot\mathbf{F}_j\right]\ . \tag{6}$$

In case of *rectlinear* flows such as linear shear, the axis of the main flow is *perpendicular* to the migration axis, i.e., $\mathbf{u}\cdot\mathbf{e}_y = 0$, so that the instantaneous velocity of *cross-stream* migration reads

$$v_m(t) = \dot{y}_c(t) = \frac{1}{\tilde{\zeta}}\sum_{i=1}^{N}\sum_{j\neq i}\mathbf{e}_y\cdot\zeta_i\ \mathbf{H}_{i,j}\cdot\mathbf{F}_j\ . \tag{7}$$

From Eq. (7) one can further define the *mean* steady-state CSM velocity, approached in the long-time limit, for each half-cycle, by averaging $v_m(t)$ over a half-period T_i, i.e.,

$$v_m^i = \langle v_m(\infty)\rangle_{T_i} = \frac{1}{T_i}\int_t^{t+T_i} dt'\ v_m(t')\ , \tag{8}$$

so that the *net* CSM velocity over a full shear cycle is simply given by $v_m = v_m^1 + v_m^2$.

For the analysis of the CSM mechanism, as discussed in the main text, it is useful to introduce a *contour-specific* migration velocity $v_m^\alpha(t)$, which can be assigned to the stiff and

bendy contour ($\alpha = s, b$) and defined via Eq. (7) as

$$v_m^\alpha(t) = \dot{y}_c^\alpha(t) = \frac{1}{\tilde{\zeta}} \sum_{i\in\alpha} \sum_{j\neq i} \mathbf{e}_y \cdot \zeta_i \, \mathbf{H}_{i,j} \cdot \mathbf{F}_j \ . \tag{9}$$

The *mean* migration velocity v_m^α of the α-contour can be determined from Eq. (8) by simply replacing $v_m(t)$ with $v_m^\alpha(t)$.

When the beads have the same radius, as in case of the ring, the drag coefficient $\zeta_i \equiv \zeta$ and $\sum_{i=1}^N \zeta_i = N\zeta$, so that Eq. (6) simplifies

$$\dot{\mathbf{r}}_c(t) = \frac{1}{N} \sum_{i=1}^{N} \left[\mathbf{u}(\mathbf{r}_i) + \sum_{j\neq i} \mathbf{H}_{i,j} \cdot \mathbf{F}_j \right] \ . \tag{10}$$

Eqs. (7) and (9) are modified accordingly.

The 2D *mean* HI-backflow $\mathbf{v}(\mathbf{r})$ at position $\mathbf{r}$ can be obtained from the instantaneous flow field

$$\mathbf{v}(\mathbf{r}, t) = \sum_{j=1}^{N} \mathbf{H}(\mathbf{r}, \mathbf{r}_j) \cdot \mathbf{F}_j \tag{11}$$

in a similar manner by using the mean forces, and shown in Fig. 3 (a) and (b) (see main text), demonstrating that the 2D profile of the backflow, as induced in the mean by the ring-forces during each shear-cycle T_i, is *elongational*.

C. Stiff Dumbbell: Zero Mean Migration

The equations of the Stokesian dynamics of bead-spring models, as provided in Section I, natively comprises also the case of an asymmetric dumbbell, composed of two beads of different radii $a_1 < a_2$ (corresponding to different drag coefficients $r_\zeta = \zeta_2/\zeta_1 > 1$) and connected by a linear spring with force constant k.

In this section we show that the *mean* cross-stream migration of a *stiff* asymmetric dumbbell at *steady state* is zero, for which purpose it is useful to rewrite the dumbbell equations in polar coordinates, starting from the full equations for each bead

$$\dot{\mathbf{r}}_1 \ = \ \mathbf{u}(\mathbf{r}_1) - \left[\frac{1}{\zeta_1}\mathbf{I} - \mathbf{H}_{1,2} \right] \cdot \mathbf{f}(R) + \mathbf{v}^{\mathrm{rot}}(\mathbf{r}_1) \ , \tag{12a}$$

$$\dot{\mathbf{r}}_2 \ = \ \mathbf{u}(\mathbf{r}_2) + \left[\frac{1}{\zeta_2}\mathbf{I} - \mathbf{H}_{2,1} \right] \cdot \mathbf{f}(R) + \mathbf{v}^{\mathrm{rot}}(\mathbf{r}_2) \ , \tag{12b}$$

where $\mathbf{u}(\mathbf{r}_{1,2})$ denote the unperturbed external flow at the bead position $\mathbf{r}_{1,2}$, while $\mathbf{v}^{\rm rot}(\mathbf{r}_{1,2})$ are the perturbations of the flow-field due to the shear-induced bead rotation, as given by Eq. (5). The matrix $\mathbf{H}(\mathbf{R}) \equiv \mathbf{H}_{1,2} = \mathbf{H}_{2,1}$ refers to the matrix elements of the Oseen-tensor, accountig for the hydrodynamic screening between the beads

$$\mathbf{H}(\mathbf{R}) = \frac{1}{8\pi\eta R}\left[\mathbf{I} + \mathbf{e}_R \otimes \mathbf{e}_R\right] \ , \tag{13}$$

with the bond unit vector $\mathbf{e}_R = \mathbf{R}/R$, the bond vector $\mathbf{R} = \mathbf{r}_1 - \mathbf{r}_2$ being the bond vector of the beads at position $\mathbf{r}_1$ and $\mathbf{r}_2$, and $R = |\mathbf{R}|$. The force $\mathbf{f}$ of the spring is measured with respect to the equilibrium bond length b

$$\mathbf{f}(R) = k(R-b)\ \mathbf{e}_R = f(R)\ \mathbf{e}_R \ . \tag{14}$$

Using the ζ-weighted center of the dumbbell ($N = 2$), i.e., $\mathbf{r}_c = \left(\zeta_1\mathbf{r}_1 + \zeta_2\mathbf{r}_2\right)/\zeta$ with $\zeta = \zeta_1 + \zeta_2$, the dynamic equations (12a) and (12b) can be rewritten as

$$\dot{\mathbf{r}}_c \ = \ \frac{1}{\zeta}\left[\zeta_1\left[\mathbf{u}_1 + \mathbf{H}(\mathbf{R})\cdot\mathbf{f}(R)\right] + \zeta_2\left[\mathbf{u}_2 - \mathbf{H}(\mathbf{R})\cdot\mathbf{f}(R)\right]\right] + \frac{1}{\zeta}\left(\zeta_1\mathbf{v}_1^{\rm rot} + \zeta_2\mathbf{v}_2^{\rm rot}\right) \ , \tag{15}$$

$$\dot{\mathbf{R}} \ = \ \mathbf{u}_1 - \mathbf{u}_2 + \mathbf{v}_1^{\rm rot} - \mathbf{v}_2^{\rm rot} - \left[\frac{1}{\zeta_1} + \frac{1}{\zeta_2}\right]\mathbf{f}(R) + 2\mathbf{H}(\mathbf{R})\cdot\mathbf{f}(R) \ . \tag{16}$$

Since we are interested in the CSM behavior of the dumbbell when it is at *steady-state*, i.e., *after* it has passed through the *transient regime*, one can drop the non-linear flow-fields $\mathbf{v}_{1,2}^{\rm rot}$ in Eqs. (15) and (16), which simplifies the following CSM analysis of a stiff dumbbell. As mentioned in the 2nd paragraph on Page 2 of Sect. I A, the flow-field $\mathbf{v}^{\rm rot}(\mathbf{r})$ is only required to assure the existence of a transient regime, so that the dumbbell can establish phase-locking and, hence, approach a steady-state *after* passing the transient. Once in steady state, the $\mathbf{v}^{\rm rot}(\mathbf{r})$-terms are no longer essential to describe the dumbbell dynamics.

Using polar coordinates of the radial and azimuthal unit vector, i.e., $\mathbf{e}_R = -(\cos\phi, \sin\phi)$ and $\mathbf{e}_\phi = (\sin\phi, -\cos\phi)$, along with $\mathbf{R} = R\ \mathbf{e}_R$, to project Eqs. (15) and (16) onto the $\mathbf{e}_R$ and $\mathbf{e}_\phi$ direction, exploiting the relation $\mathbf{H}(\mathbf{R})\cdot\mathbf{e}_R = (4\pi\eta R)^{-1}\mathbf{e}_R$ and Eq. (4), one obtains four, coupled, non-linear equations, describing the dumbbell dynamics in polar coordinates

$$\dot{\phi} \ = \ -S(t)\sin^2\phi\,, \tag{17}$$

$$\dot{R} \ = \ \frac{1}{2}S(t)R\sin(2\phi) - f(R)\left[\frac{1}{\zeta_1} + \frac{1}{\zeta_2} - \frac{1}{2\pi\eta R}\right] \ , \tag{18}$$

$$\dot{y}_c \ = \ \frac{\zeta_2 - \zeta_1}{\zeta_1 + \zeta_2}\frac{f(R)}{4\pi\eta R}\sin\phi \equiv v_m(t)\,, \tag{19}$$

$$\dot{x}_c \ = \ S(t)y_c + \frac{\zeta_2 - \zeta_1}{\zeta_1 + \zeta_2}\frac{f(R)}{4\pi\eta R}\cos\phi\,. \tag{20}$$

Importantly, in the numerical simulation of the dumbbell with the respective results shown in the main text [see Fig. 1 (a)] and in Sections II A, II B, and V A of the SI, the flows $\mathbf{v}^{\rm rot}(\mathbf{r}_{1,2})$ have been taken into account.

Equation (19) describes the instantaneous migration velocity $v_m(t) \equiv \dot{y}_c(t)$ of the dumbbell and with $f(R) = k(R-b)$, cf. Eq. (14), leads to the final expression of Eq. (3), as given in the main text. The *net* migration step per half period $T/2$ can be obtained by integrating Eq. (19) over a half period

$$\Delta y_c = \int_t^{t+T/2} dt'\; v_m(t') = \frac{k}{4\pi\eta}\frac{r_\zeta - 1}{r_\zeta + 1} \int_t^{t+T/2} dt'\; \frac{R(t') - b}{R(t')}\; \sin\phi(t')\,. \tag{21}$$

When the dumbbell is rigid, the bond length does not change ($\dot{R} = 0$) and is fixed to the equilibrium bond length $R = b$. This condition imposes a constraint on the dumbbell dynamics, resulting in a constraining force $f(R)$ which can be determined from Eq. (18)

$$f(R=b) = \frac{S(t) b \sin 2\phi}{2\left(\frac{r_\zeta+1}{\zeta_2} - \frac{1}{2\pi\eta b}\right)}\,. \tag{22}$$

The shear rate $S(t)$ in Eq. (22) can be replaced via Eq. (17), so that the constraint force $f(b)$, appearing in Eq. (19), can be eliminated. We then obtain an expression for the migration step per half cycle, which depends only on the orientation ϕ_1 and ϕ_2 at the beginning, respectively, end of a half-cycle

$$\Delta y_c = -\underbrace{\frac{1}{8\pi\eta}\frac{r_\zeta - 1}{r_\zeta + 1}\frac{1}{\left(\frac{r_\zeta+1}{\zeta_2} - \frac{1}{2\pi\eta b}\right)}}_{=:C} \int_{\phi_1}^{\phi_2} d\phi \frac{\sin 2\phi}{\sin\phi} = -2C \int_{\phi_1}^{\phi_2} d\phi \cos\phi = 2C\left[\sin\phi_1 - \sin\phi_2\right] \tag{23}$$

Using Eq. (23) one can now determine the *net* migration step for a full shear cycle by simply adding the respective steps for each half cycle. During the first half period $T/2$, the orientation angle ϕ of the dumbbell changes from $\phi_1 \to \phi_2$ where the dumbbell migrates the step

$$\Delta y_c^{(1)} = 2C\left[\sin\phi_1 - \sin\phi_2\right]\;. \tag{24}$$

During the second half of the shear cycle, the dumbbell swings back and reverses its orientation back from $\phi_2 \to \phi_1$, and the dumbbell performs the step

$$\Delta y_c^{(2)} = 2C\left[\sin\phi_2 - \sin\phi_1\right] = -\Delta y_c^{(1)}\;. \tag{25}$$

From Eqs. (24) and (25) follows that the magnitude of the migration steps are the same, but have the opposite sign. Therefore, when the dumbbell is *rigid* the *net* migration over a full shear cycle vanishes, i.e., $\Delta y_c = \Delta y_c^{(1)} + \Delta y_c^{(2)} = 0$.

D. Capsule (3D)

The Lattice-Boltzmann (LB) method is a mesoscopic method for solving fluid problems which is based on a discretization of space and velocities. Over the last years it has become a well-established method and we omit the details which can be found in e.g.[4–6]. We use the D3Q19 scheme as implemented in the ESPResSo package[7,8].

For the elastic capsule, we implemented the immersed boundary method into ESPResSo, following the work of Refs.[9,10]. The surface of the particle is discretized into 1280 triangles and endowed with an elastic shear and a bending resistance. The elastic force is described by the Neo-Hookean law and the bending resistance by a Helfrich Hamiltonian[11]. We add an additional force to ensure volume conservation as in[10].

The x-z periodic LB-grid has a size of $120 \times 180 \times 120$ lattice units and is bounded by walls in the y direction. A linear shear flow is imposed by moving the upper and lower walls in opposite directions with a fixed velocity. The physical length and time scales are chosen such that the grid dimension in SI units is $720 \times 1080 \times 720$ μm^3, the density and kinematic fluid viscosity are 1000 kg/m^3 and 10^{-6} m^2/s, respectively (corresponding to water); the frequency is 1.75 Hz, the shear rate is 22.22 s^{-1}, and the time step is 10.8 μs.

The particle has a radius of 39.6 μm, a bending resistance in the soft half of $9.2 \cdot 10^{-17}$ Nm, and an elastic modulus of $4.4 \cdot 10^{-5}$ N/m. For comparison, the typical values for a red blood cell are 4 μm radius, $2 \cdot 10^{-19}$ Nm bending resistance, and $5 \cdot 10^{-6}$ N/m elastic modulus. A typical timescale for the capsule relaxation can be defined via $\tau_b = \eta a^3/\kappa_2$.

Table II lists the respective parameters for the 3D capsule (radius a, bending stiffness $\kappa_{1,2}$), and the shear flow (shear rate $\dot{\gamma}$, period T, viscosity η) used in the simulation. The conversion of each parameter "Q" between the "SI" units and "sim" units is realized by multiplying Q^{SI} with the powers of the conversion parameters for time C_t, length C_x, and density C_ρ; for example, the dynamic viscosity $\nu^{\mathrm{SI}} = \nu^{\mathrm{sim}} \cdot {\mathrm{C}_x}^2/\mathrm{C}_t$, so that $[\nu] = \mathrm{m}^2/\mathrm{s}$. Here, we choose $\mathrm{C}_x = 6.0 \cdot 10^{-6}$ m, $\mathrm{C}_t = 36.0 \cdot 10^{-5}$ s, and $\mathrm{C}_\rho = 10^3$ kg/m^3 to prescribe a micrometer length scale, and the fluid density and viscosity to resemble that of water.

TABLE II: Parameters used in the simulation of the 3D capsule.

particle kind	a	$\kappa_{1,2}$	$\dot{\gamma}$	T	η
capsule (SI units)	39.6 μm	$9.2 \cdot 10^{-17}/13.8 \cdot 10^{-17}$ Nm	22.22 s^{-1}	0.57 s	10^{-3} Pas
capsule (sim. units)	6.6	1.53/2.3	0.008	1590	10.0

II. GENERIC BEHAVIOR OF CROSS-STREAM MIGRATION (CONTINUED)

A major outcome of this study is that the cross-stream migration of all three kinds of particles behaves *qualitatively* the same, irrespective of the model details and dimensionality of the particle, which lets us conclude that the CSM is a *generic* property.

Here we show that the CSM characteristics in terms of *orientation robustness* and *frequency dependence*, discussed via Fig. 4 and 5 of the main text by example of the ring-polymer (2D), are also displayed by the dumbbell (1D) and the capsule (3D).

A. Orientation Robustness of the Dumbbell (1D) and Capsule (3D)

Figure 1 shows the dependence of the migration velocity $\langle v_m(t)\rangle_T$ of the (left) dumbbell and (right) capsule, averaged over the period T, as a function of time $t\dot{\gamma}$ for different initial orientations ϕ_0. In case of the dumbbell, ϕ_0 is taken from the ϕ_0-intervals $I^+ = [1.1; 2.0]\,\pi$ and $I^- = [0.1; 1.0]\,\pi$, where $I^{+/-}$ denotes the interval leading to a positive or negative v_m, respectively. For the capsule, the corresponding intervals are given by $I^+ = [1.5; 2.25]\,\pi$ and $I^- = [0.5; 1.25]\,\pi$ and quantitatively differ to those of the dumbbell and the ring-polymer.

Similar to the 2D ring (see main text, Fig. 4), the migration velocity $\langle v_m(t)\rangle_T$ of the dumbbell and capsule depends on ϕ_0 within a transient regime and approaches a steady-state, common value $v_m \equiv \langle v_m(\infty)\rangle_T$ in the long-time limit, independent of ϕ_0 in each case. Again, the sign of v_m depends on whether ϕ_0 is taken from the interval I^+ or I^-; the width of both intervals is with $\Delta I^{+/-} \approx \pi$ rather large, so that the terminal CSM velocity v_m of the 1D dumbbell and 3D capsule is quite robust against uncertainties in ϕ_0, consistent with the CSM behavior of the 2D ring (see main text, Fig. 4).

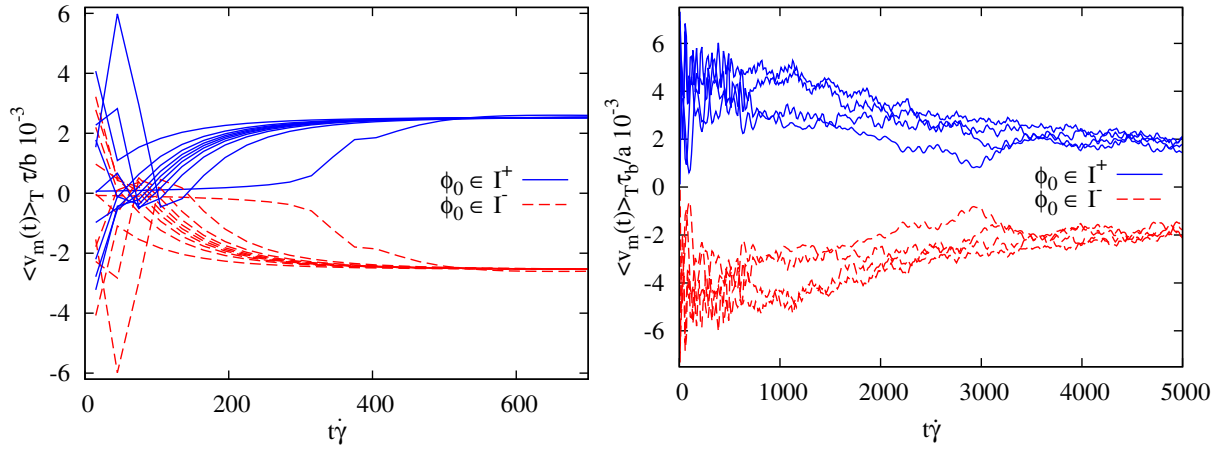

FIG. 1: (Color online) T-averaged migration velocity $\langle v_m(t)\rangle_T$ vs. time $t\dot{\gamma}$ shown for the 1D dumbbell (left) and 3D capsule (right). In each case, the 2π-range of ϕ_0 can be grouped in two intervals I^+ and I^-, leading to a positive or negative v_m. The intervals $I^{+/-}$ are: (left) dumbbell: $I^+ = [1.1; 2.0]\,\pi$ and $I^- = [0.1; 1.0]\,\pi$, (right) capsule: $I^+ = [1.5; 2.25]\,\pi$ and $I^- = [0.5; 1.25]\,\pi$.

B. Frequency Dependence of the Dumbbell (1D) and Capsule (3D)

Figure 2 shows the dependence of the migration velocity v_m versus the period $T\dot{\gamma}$ (inverse frequency) with $\dot{\gamma}$ fixed. Also here, about four dynamic regimes can be identified for the (left) 1D dumbbell and (right) 3D capsule, depending on the period T similar to the 2D ring- polymer (see main text, Fig. 5). The v_m-T behavior of the capsule can be characterized in the same manner as for the ring due to the close resemblance of the two systems, namely a combination of shear deformation at low frequency and a setting in of a tank-treading dynamics at medium and large frequencies.

For the dumbbell, a classification in terms of a shear- and tank-treading dynamics is not adequate, since the "shape" of the dumbbell with $N = 2$ beads can not be associated with a proper contour as opposed to the 2D/3D particles. Instead, the dumbbell dynamics should be described in terms of a *stretch-compress* dynamics of the bond length along with a *pendulous* and *rotational* motion.

The analogy between the 1D and 2D/3D systems consists then in identifying the dumbbell's shear-induced pendulous dynamics (back- and forward swing cycles along with the stretch-compress cycle of the bond length) with the oscillatory shear deformation (low frequency) of the ring and capsule, respectively, and accordingly the dumbbell rotation with tank-treading (medium/large frequency).

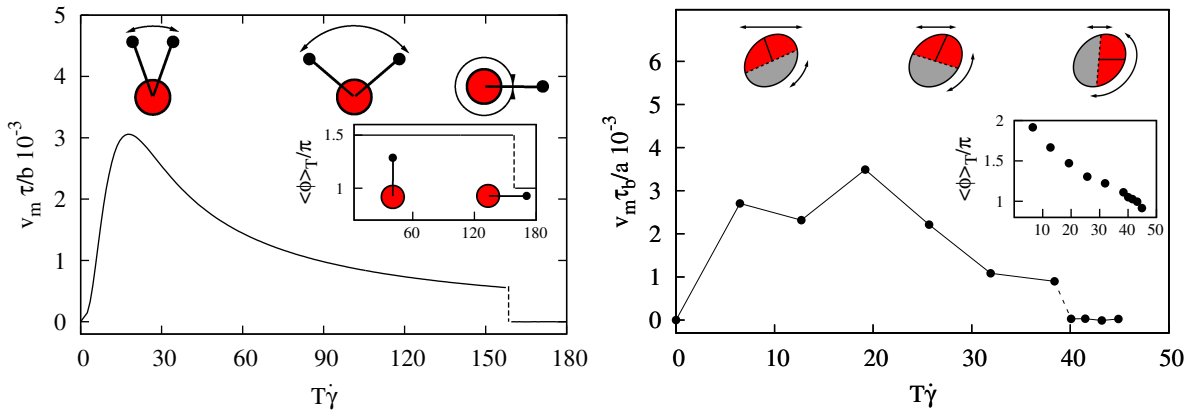

FIG. 2: (Color online) Migration velocity v_m versus switching period $T\dot{\gamma}$ (inverse frequency), shown for the 1D dumbbell (left) and 3D capsule (right) with four dynamic regimes: (1) oscillatory motion (pendular/shear deformation) at small T (high frequency), (2) weak rotational/tank-treading motion superposed with (1) (mid frequency), (3) enhanced rotational/tank-treading dynamics at large T (low frequency), and (4) zero net migration. Insets: T-averaged mean orientation $\langle\phi\rangle_T$ vs. $T\dot{\gamma}$ of the dumbbell and the capsule, respectively. At high frequency, the dumbbell (capsule) orientation $\langle\phi\rangle_T \approx 1.5\pi$ (1.5π), i.e., the small ζ_1 (stiff κ_2-contour) remains in the mean in the upper half-space ($v_m > 0$). Once $T\dot{\gamma} > 160$ (40), the mean orientation flips to $\langle\phi\rangle_T \approx \pi$ (π), i.e., the dumbbell (capsule) orientation has an upper-lower symmetry ($v_m = 0$).

What matters for the cross-stream migration is that the asymmetric parts of each type of particle reside in the *mean* in one of the half-spaces when the frequency is high (small T), whereas at medium and in particular at low frequency (large T) there is a "re-shuffling" of the differing constituents (in terms of friction coefficient or stiffness) between the two half-spaces; whether this re-shuffling occurs via rotation (dumbbell) or tank-treading (ring, capsule) is irrelevant and leads to the *same qualitative*, i.e., generic behavior for all three kinds of particles (see main text: Fig. 4 and 5 and SI: Fig. 1 and 2, respectively).

III. SAMPLE MOVIES: ILLUSTRATION OF MIGRATION REGIMES

The MP4-format movies, cf. Table III, show the shear-induced dynamics for each particle kind in the typical CSM regime with the values for $T\dot{\gamma}$ given in Table III. For each case, these values are chosen in accord with the v_m-$T\dot{\gamma}$ curves of Fig. 5 (main text: 2D ring) and Fig. 2 (SI: 1D dumbbell and 3D capsule), starting with small values of $T\dot{\gamma}$ (high frequency), followed by medium $T\dot{\gamma}$-values (mid frequency), and finally large periods (low

frequency). The movie set M1-M9 visualize how the particle dynamics traverses from the

TABLE III: MPEG movies M1-M9 visualizing the migration dynamics characteristic for each regime. For each movie "M#:" the value of $T\dot{\gamma}$ used in the simulation is given.

particle kind	pen/def	pen/def+rot/TT	rot/TT
dumbbell	M1: 5	M2: 100	M3: 180
ring	M4: 2	M5: 10	M6: 12
capsule	M7: 6	M8: 26	M9: 45

pendulous/deformation (pen/def) regime at high frequency (small $T\dot{\gamma}$) to the rotation/tank-treading (rot/TT) dominated regime at low frequency (large $T\dot{\gamma}$).

IV. ORIGIN OF ABRUPT CSM-DROP: $\langle\phi(t)\rangle_T$ PHASE-SPACE ANALYSIS

In this section, we extend our brief discussion of the abrupt v_m-drop (see main text: Fig. 5 and SI: Fig. 2) and provide here a more in-depth analysis. As already discussed in detail in the main text, the cross-stream migration $v_m = \langle v_m(\infty)\rangle_T$ is intimately correlated with the *mean* steady-state orientation $\langle\Phi\rangle_T \equiv \langle\phi(\infty)\rangle_T$, acquired by the particle over the course of *one* shear cycle and can be tuned via the external control parameter $T\dot{\gamma}$. Figure 5 (main text) and Fig. 2 (SI) demonstrate this close relationship for all three particles, how the mean particle orientation is the key controlling factor for the presence or absence of CSM[13]. In case of the ring, cf. Fig. 5 (main text), such a change of v_m occurs once the period $T\dot{\gamma}$ exceeds a critical value $T_c\dot{\gamma} \approx 11$.

In order to gain a better insight on why the particles alter their *stable mean* orientation when the switching period T is varied, we determine numerically the phase-space of the time-dependent *mean* orientation $\langle\dot{\phi}(t)\rangle_T$-$\langle\phi(t)\rangle_T$, obtained by launching the particle at *different* initial orientations ϕ_0 over the entire interval $\phi_0 \in [0.0, 2.0]\ \pi$, and keeping the switching period $T\dot{\gamma}$ fixed. This procedure is then repeated at different (but fixed) values of $T\dot{\gamma}$. Such a phase-plot allows one then to analyze and identify in general the set of *stable* mean orientations (attractors) the particle can adopt[12]. In accord with the discussion in the main text, we use again the ring-polymer as representative particle.

Figure 3 shows such a phase-space plot for the ring (following the above procedure) for three different values of the switching period around the critial value $T_c\dot{\gamma} \approx 11$, where the

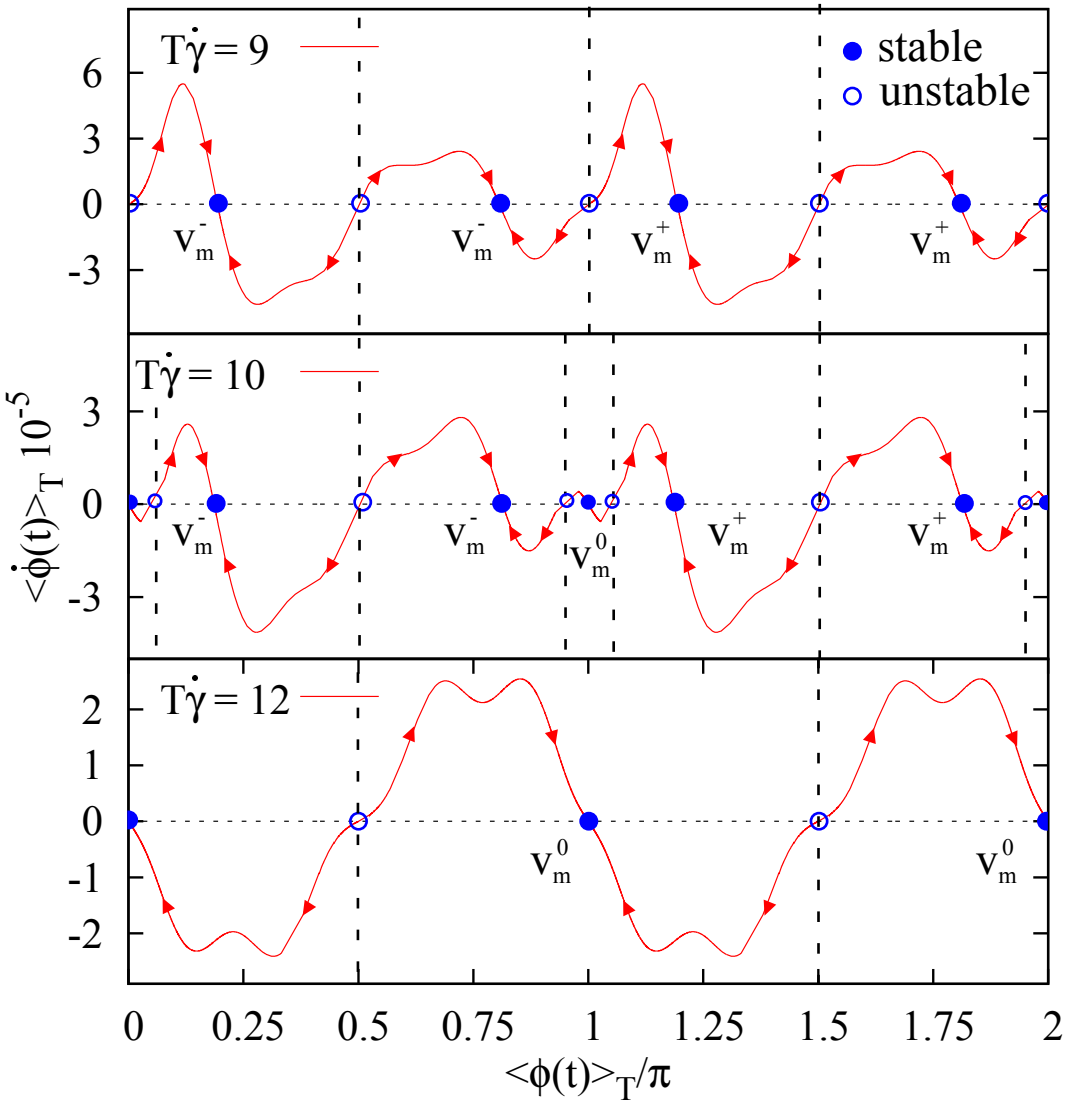

FIG. 3: (Color online) Phase-space of the time-dependent mean orientation $\langle\dot{\phi}(t)\rangle_T - \langle\phi(t)\rangle_T$ for the same ring, as in Fig. 5 (main text) at three different values of the switching period $T\dot{\gamma} = 9$, 10, and 12, around the critical value $T_c\dot{\gamma} \approx 11$, marking the onset of the abrupt change of the ring orientation. For each value of $T\dot{\gamma}$, there is a distinct set of stable (symbol: •) and unstable (symbol: ◦) fixed points ($\langle\dot{\phi}\rangle_T = 0$). The stable fixed points (FP) correspond to non-migrating (v_m^0) orientations with $\langle\phi\rangle_T^0 = \{0.0, 1.0\}$ π or (positive/negative) migrating states ($v_m^{+/-}$) with a mean orientation $\langle\phi\rangle_T^{+/-}$ other than 0.0 π and π. The switching period $T\dot{\gamma}$ sensitively controls whether migrating and non-migrating orientations coexist ($T\dot{\gamma} = 10$) or not ($T\dot{\gamma} = 9$ and 12). The angular interval between neighboring *unstable* FPs define the range of an asymptotically stable FP, as marked by the dashed lines. When the transient angle $\langle\phi(t)\rangle_T$ lies within the range of a specific stable FP, the ring approaches the mean orientation $\langle\phi\rangle_T^{FP}$ of this fixed point.

abrupt change of the mean orientation occurs, i.e., $T\dot{\gamma} = 9$, 10, and 12. From the phase-space plot shown in Fig. 3 one can easily determine the so-called orientation *fixed points* (FP) of the system, which refer to those mean orientations $\langle\phi\rangle_T^{FP}$ where $\langle\dot{\phi}\rangle_T = 0$, as marked by the symbols $\bullet$ and $\circ$ in each case. Whether an FP is *stable* (symbol: $\bullet$) or *unstable* (symbol: $\circ$) depends on the slope $\beta = d\langle\dot{\phi}\rangle_T/d\langle\phi\rangle_T$ near the FP. If $\beta < 0$, the FP is *asymptotically stable* and the orientation $\langle\phi(t)\rangle_T$ moves towards the orientational fixed-point $\langle\phi\rangle_T^{FP}$, as long as $\langle\phi(t)\rangle_T$ lies within the range of the (orientational) attractor, while it moves away from the FP if $\beta > 0$. The respective FP is then *unstable*[12]. Near the fixed point, this behavior can be formally described by $d_t\langle\phi(t)\rangle_T = \langle\dot{\phi}(t)\rangle_T \approx \beta\left[\langle\phi(t)\rangle_T - \langle\phi\rangle_T^{FP}\right]$ with $d_t = d/dt$, reflecting the exponential behavior towards or away from the FP.

Applying these general concepts to the three different phase-space plots of Figure 3, one can identify a total of 8 FPs when $T\dot{\gamma} = 9$, among which the 4 orientations $\langle\phi\rangle_T^{FP} \in I_{FP}^{<} = [0.25, 0.8, 1.25, 1.8]\ \pi$ are asymptotically stable ($\beta < 0$) and the other ones are unstable ($\beta > 0$). Importantly, the *range* of each attractor (marked by the vertical dashed lines) is about 0.5 π, so that for a given initial orientation $\phi_0 \in [0.0, 2.0]\ \pi$ the transient ring orientation $\langle\phi(t)\rangle_T$ evolves towards *one* of these available stable FPs and acquires its affiliated steady-state *mean* orientation $\langle\phi\rangle_T^{FP} \in I_{FP}^{<}$, when $\langle\phi(t)\rangle_T$ lies within the range of this attractor. We note that while in general for any (but fixed) value of $T\dot{\gamma}$ all FPs are available to the particle, it can accept only *one* orientational fixed point for only *one* initial angle ϕ_0. As discussed in the main text, the existence and direction of the CSM depends on the mean steady state particle orientation $\langle\phi\rangle_T = \langle\phi(\infty)\rangle_T$, controlling whether the stiff/bendy contour portions reside in the *mean* within the upper and lower half-space.

When $T\dot{\gamma} = 9$, the ring can only adopt the mean orientations $\langle\phi\rangle_T \in I_{FP}^{<} = [0.25, 0.8, 1.25, 1.8]\ \pi$, which correspond to migrating orientations only with $v_m^{+/-} \neq 0$, cf. Fig. 3 (top). Two of these states, i.e., $\langle\phi\rangle_T^{+} = [1.25, 1.8]\ \pi$, lead to a *positive* migration ($v_m^{+} > 0$) since the stiff/bendy part of the ring contour reside in the mean in the upper/lower half-space (as discussed in the main text.), and vice versa for the two remaining states $\langle\phi\rangle_T^{-} = [0.25, 0.8]\ \pi$. Note that within each class of stable states $\langle\phi\rangle_T^{+/-}$ the CSM steady state velocity v_m is the same, while the respective mean orientation is different.

When the period is further increased to $T\dot{\gamma} = 10$, but still lower than the critical value $T_c\dot{\gamma} = 11$, the previous set of fixed points in terms of their *value* remains, while four new FPs appear at around $[0.1, 0.9, 1.1, 1.9]\ \pi$, all of which are *unstable*, cf. Fig. 3 (middle).

Importantly, the two previously unstable FPs at $\langle\phi\rangle_T^{FP} = \pi$ and 2.0 π reverse their character and become now *stable* fixed points (attractors). Since these mean orientations have an upper-lower symmetry where an equal amount of the stiff and bendy contour are located in the mean within the upper and lower half-space, these states refer to *non-migrating* orientations ($v_m^0 = 0$). For the initial ring orientation of $\phi_0 = 2.0\ \pi$, the ring does not approach the new non-migrating FP $\langle\phi\rangle_T^{FP} = 2.0\ \pi$, but still locks-in to the "old" migrating fixed point $\langle\phi\rangle_T^{FP} = 1.8\ \pi$, as shown in the $\langle\phi\rangle_T$-$T\dot{\gamma}$ plot of Fig. 5 (inset: main text). This occurs because over the course over many shear cycles, the transient angle $\langle\phi(t)\rangle_T$ of the ring does not lie within the narrow range of the 2π-attractor, but is located within the range of the FP $\langle\phi\rangle_T^{FP} = 1.8\ \pi$, which has a broad stability range of about 0.5 π, cf. Fig. 3 (middle).

When the period exceeds the critical value $T\dot{\gamma} > T_c\dot{\gamma} = 11$, the coexistence of migrating and non-migrating states vanishes entirely, and only a total of 4 fixed points remain, as shown in Fig. 3 (bottom). The respective two asymptotically stable FPs with the mean steady-state orientation $\langle\phi\rangle_T^{FP} \in I_{FP}^{<} = [1.0, 2.0]\ \pi$ are all *non-migrating* states v_m^0. Simultaneously, their attractor range has substantially grown from about 0.1 π ($T\dot{\gamma} = 10$) to π ($T\dot{\gamma} = 12$).

The abrupt drop of the migration velocity v_m is therefore a direct consequence of its strong link to the *mean* orientation $\langle\phi\rangle_T$, leading to a discrete sequence of migrating ($v_m^{+,-}$) or non-migrating (v_m^0) states, which may even coexist. The number and type of these stable states $\langle\phi\rangle_T^{FP}$ (attractors) can be externally tuned by the control parameter $T\dot{\gamma}$ with the result that the entire attractor landscape changes, including the appearance/disappearance of new/old FPs or the reversal of stable FPs to unstable ones and vice versa. In case of the ring and an initial orientation of $\phi_0 = 2.0\ \pi$ this means that the orientational attractor $\langle\phi\rangle_T^{FP} = 1.8\ \pi$ disappears once $T\dot{\gamma} > T_c\dot{\gamma} \approx 11$, so that $\langle\phi(t)\rangle_T$ adopts the orientation 1.8 π only transiently while a new stable orientational fixed point emerges at $\langle\phi\rangle_T^{FP} = 2.0\ \pi$. Since the value 1.8 π lies within the (extended) range of the 2π-attractor, the orientation $\langle\phi(t)\rangle_T$ approaches this new fixed point, corresponding to a non-migrating state. Hence, at the critical value of $T_c\dot{\gamma} = 11$, there is a discontinuous transition of the ring mean orientation $\langle\phi\rangle_T^{FP}$ from a v_m^+-migrating state to a v_m^0-non-migrating one, and appears in the v_m-$T\dot{\gamma}$ plot as abrupt drop of v_m, as shown in Fig. 5 (main text).

V. CSM-ROBUSTNESS AGAINST VARIATIONS OF TILT-ANGLE Θ

In Fig. 4 (main text) and in Fig. 1 (SI: Sect. II A) we have shown that $v_m > 0$ when the initial orientation $\phi_0 \in I^+$, and $v_m < 0$ for $\phi_0 \in I^-$. In all these cases we assumed that the *second* angle (tilt angle θ), determining the particle orientation outside the x-y shear plane, is zero, as indicated in the particle sketches of Fig. 1 (a)-(c) (see main text).

In general, however, one must expect that the direction of the CSM (sign of v_m) does not only depend on the initial *in-plane* orientation (specified by $\phi_0 \in I^{\pm}$), but also on the θ_0-orientation outside the y-x shear plane.

In the following sections we show that the cross-stream behavior, as characterized by the finite slope of the lateral position $y_c(t)$ corresponding to a finite migration velocity $v_m \neq 0$, persist and remains *robust* for all three particles, if their initial orientation $\{\phi_0, \theta_0\}$ is allowed to vary also away from the shear plane ($\theta_0 \neq 0.0$).

A. Dumbbell (1D)

Figure 4 (left) shows the lateral position $y_c(t)$ vs. time for the 1D dumbbell at varying tilt-angles $\theta_0 \in [0.0, 0.5]\ \pi$ outside the y-x shear plane and an in-plane initial orientation of $\phi_0 = 2.0\ \pi$. The CSM behavior persist over the entire range of θ_0-orientations with $\theta_0^+ \in I^+ = [0.0, 0.5[\ \pi$, leading to a positive cross-stream migration (v_m^+). Only for the single tilt angle $\theta_0^0 = 0.5\ \pi$, the CSM vanishes as reflected by the zero slope of $y_c(t)$.

Figure 4 (right) shows the respective time-dependence of $\theta(t)$, which approaches $\theta(\infty) \approx 0.0\ \pi$ for long times if $\theta_0^+ \in I^+$. In these cases, the dumbbell reorients back towards the stable orientation $\theta(t) \to 0.0\ \pi$, i.e., the dumbbell axis lies within the y-x shear plane. The tilt angle $\langle\theta\rangle_T^{FP} = 0.0\ \pi$ refers therefore to an *asymptotically stable* fixed point (FP)[12].

In turn, for $\theta_0 = 0.5\ \pi$ the tilt angle remains constant (unstable FP) since the dumbbell lies within the z-x plane (this plane is perpendicular to the shear plane), in which case the shear is ineffective as the dumbbell has no lateral extension (zero thickness) and $v_m = 0$.

Overall, the CSM-effect of the dumbbell is quite *robust* against a broad variation of the initial orientations with regards to ϕ_0 and θ_0.

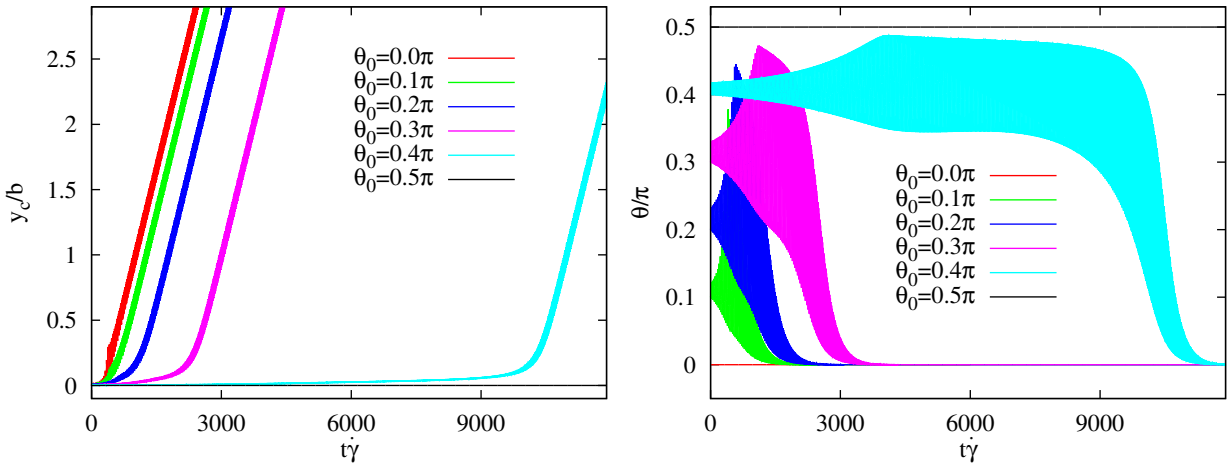

FIG. 4: (Color online) Robustness of the CSM for the 1D dumbbell in regards to variations of the tilt angle θ_0 outside the y-x shear plane with $\theta_0 \in [0.0, 0.5]\ \pi$; the initial in-plane orientation is $\phi_0 = 2.0\ \pi$. Left: Lateral position $y_c(t)$ vs. time $t\dot{\gamma}$, displaying the persistence of the CSM effect ($v_m^+ > 0$) for the entire range of θ_0-orientations with $\theta_0^+ \in I^+ = [0.0, 0.5[\ \pi$. Only for $\theta_0 = 0.5\ \pi$, the CSM is zero. Right: Time-dependence of the respective tilt angle $\theta(t)$, showing how the dumbbell axis reorients back towards the stable orientation within the y-x shear plane ($\theta(\infty) = 0.0\ \pi$) if $\theta_0^+ \in I^+$. When $\theta_0 = 0.5\ \pi$ the dumbbell retains this orientation.

B. Ring (2D)

In contrast to the 1D dumbbell and 3D capsule, both of which have an axis of *high rotational symmetry*, the 2D ring-polymer has only a twofold 180^o-symmetry since it is *planar*, so that the ring can be tilted outside the y-x shear plane in two ways, namely by rotating its plane either along the x- or y-axis.

Figure 5 (left) shows the lateral position $y_c(t)$ vs. time for the 2D ring with its plane being rotated along the x-axis (top) and y-axis (bottom), respectively, at varying tilt-angles $\theta_0^{x,y} \in [0.0, 0.5]\ \pi$ outside the y-x shear plane and an in-plane initial orientation of $\phi_0 = 2.0\ \pi$.

Similar to the dumbbell, the CSM behavior of the ring also persist over the entire range of $\theta_0^{x,y}$-orientations with $\theta_0^+ \in I^+ = [0.0, 0.5[\ \pi$, leading to a positive cross-stream migration ($v_m^+ > 0$), irrespective along which axis the ring plane is rotated. Only for the single tilt angle $\theta_0^0 = 0.5\ \pi$, the ring does not migrate. However, contrary to the dumbbell and capsule, there is no longer a common steady-state migration velocity v_m^+ in the long-time limit, but depends on the initial tilt angle θ_0^+.

Figure 5 (right) shows for either case the respective time-dependence of $\theta^{x,y}(t)$, which

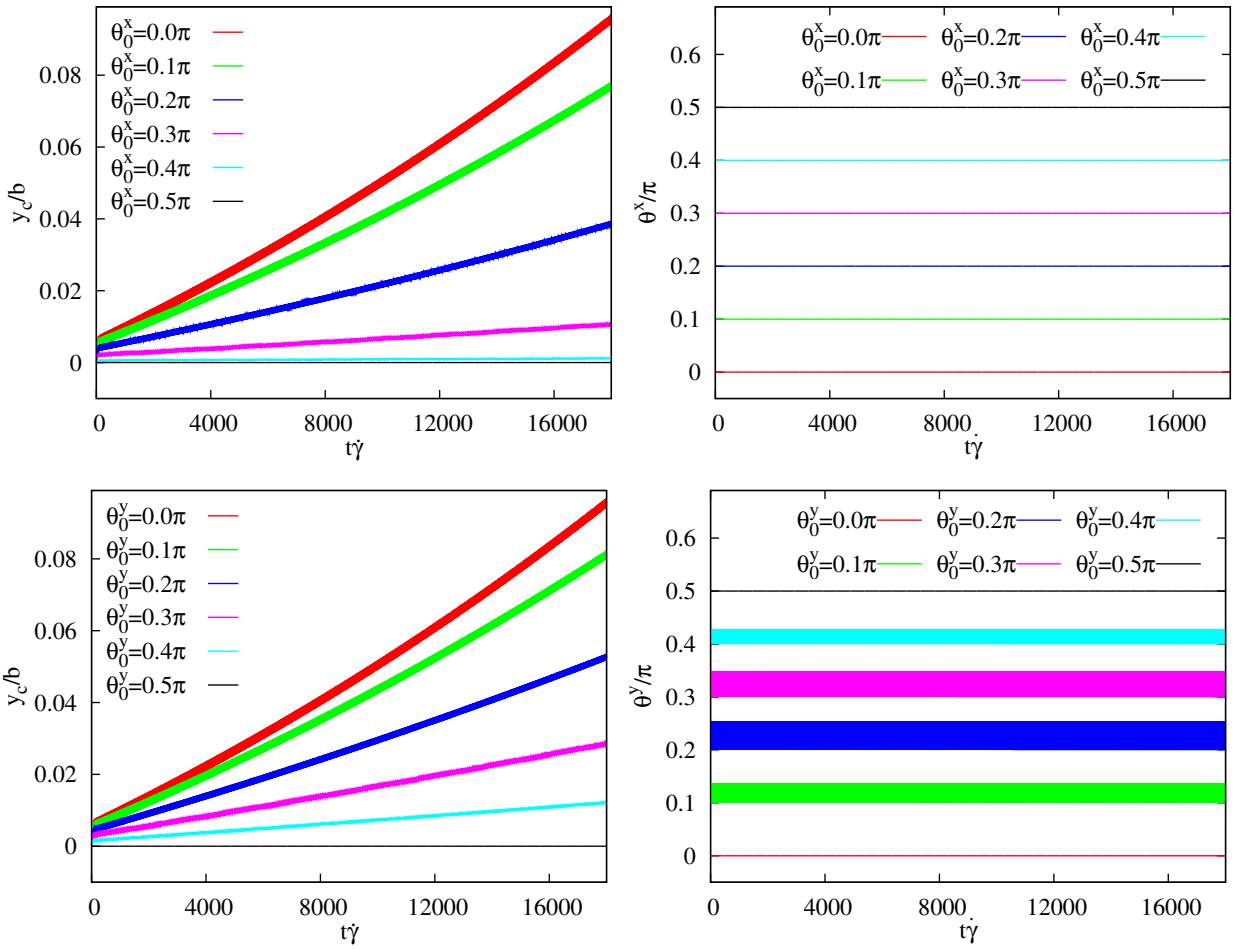

FIG. 5: (Color online) Robustness of the CSM for the 2D ring with respect to θ_0-variations outside the y-x shear plane, and an initial in-plane orientation of $\phi_0 = 2.0\ \pi$ (similar to Fig. 1 (b): see main text). The top panel refers to θ_0^x-orientations, where the ring plane is rotated along the x-axis, and the bottom panel refers to θ_0^y-orientations. Left: Lateral position $y_c(t)$ vs. scaled time $t\dot{\gamma}$, displaying the persistence of the CSM effect ($v_m > 0$) for the entire range of off-plane orientations $\theta_0^{x,y} \in [0.0, 0.5[\ \pi$. Only when $\theta_0^{x,y} = 0.5\ \pi$, the CSM is zero. Right: Time dependence of the respective off-plane orientation $\theta^{x,y}(t)$ starting at $\theta_0^{x,y}$, showing that the off-plane orientation of the ring $\theta^{x,y}(t)$ remains in the mean constant.

remains constant for all times, while the ring continues to migrate within the y-x shear plane. Hence, the ring plane does not reorient back towards the y-x shear plane as the dumbbell and capsule do, but holds its initial orientation $\theta_0^{x,y}$. In this case, all angles $\langle\theta\rangle_T^{FP} = \theta_0^{x,y} \in [0.0, 0.5]\ \pi$ are so-called *neutral stable* fixed points $\langle\dot{\theta}\rangle_T = 0$[12].

Overall, the CSM-effect of the ring is quite *robust* against a broad variation of the initial orientations with regards to ϕ_0 and θ_0.

C. Capsule (3D)

Finally, we show in Fig. 6 (left) the lateral position $y_c(t)$ vs. time for the 3D capsule at varying tilt-angles $\theta_0 \in [0.0, 0.5]\ \pi$ outside the y-x shear plane and an in-plane initial orientation of $\phi_0 = 2.0\ \pi$. Similar to the 1D and 2D particle, the CSM behavior persist also for the 3D capsule over a broad range of θ_0-orientations outside the shear plane with $\theta_0^+ \in I^+ = [0.0, 6/18]\ \pi$, leading to a positive cross-stream migration (v_m^+). When $\theta_0^0 \in I^0 = [7/18, 0.5]\ \pi$, the CSM vanishes in the long-time limit, as reflected by the flattening of $y_c(t)$.

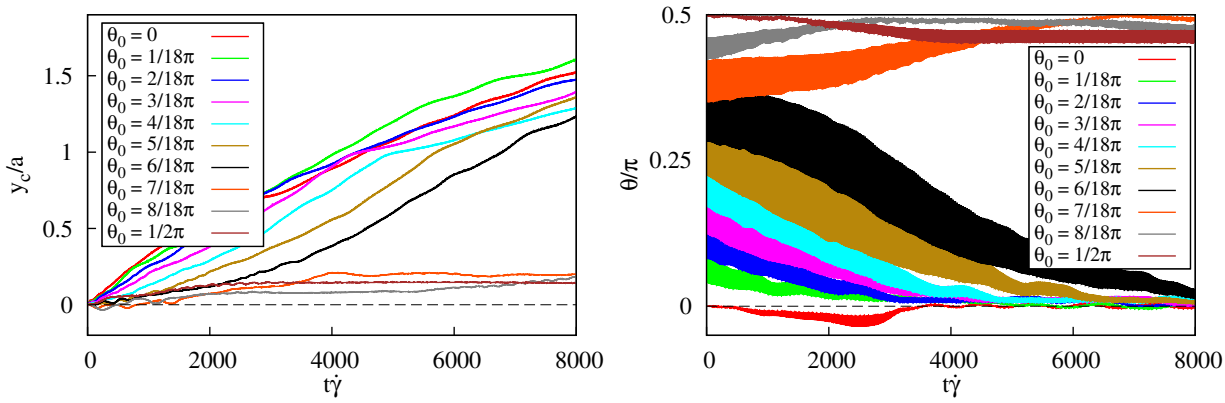

FIG. 6: (Color online) Robustness of the CSM for the 3D capsule in regards to variations of the tilt angle θ_0 outside the y-x shear plane with $\theta_0 \in [0.0, 0.5]\ \pi$; the initial in-plane orientation is $\phi_0 = 2.0\ \pi$. Left: Lateral position $y_c(t)$ vs. time $t\dot{\gamma}$, displaying the persistence of the CSM effect ($v_m^+ > 0$) for a broad range of θ_0-orientations with $\theta_0^+ \in I^+ = [0.0, 6/18]\ \pi$. For other orientations $\theta_0^0 \in I^0 = [7/18, 0.5]\ \pi$ the CSM is nearly zero. Right: Time-dependence of the respective tilt angle $\theta(t)$ showing how the capsule axis reorients back towards the stable orientation within the y-x shear plane ($\theta(\infty) \approx 0.0\ \pi$) if $\theta_0^+ \in I^+$. For $\theta_0^0 \in I^0$ the tilt angle approaches another stable orientation $\theta(\infty) = 0.5\ \pi$, corresponding to a state with an upper-lower symmetry, so that $v_m = 0$.

Figure 6 (right) shows the respective time-dependence of $\theta(t)$, which approaches in the long-time limit towards the steady-state angle $\theta(\infty) \approx 0.0\ \pi$ when the initial tilt angle is $\theta_0^+ \in I^+$. This implies that for these θ_0^+-orientations the capsule preferential stable orientation at steady-state is such that its axis lies within the y-x shear plane. In turn, for $\theta_0^0 \in I^0$ the tilt angle approaches another possible stable orientation $\theta(\infty) \approx 0.5\ \pi$, in which case the capsule axis lies now within the z-x plane (the plane being perpendicular to the

shear-plane). This orientation corresponds to a state with an *upper-lower* symmetry, so that in the mean $v_m = 0$. In case of the capsule, there are now two *asymptotically stable* fixed points (FP) at $\langle\theta\rangle_T^{FP} = 0.0\ \pi$ and $0.5\ \pi$[12].

Overall, the CSM-effect of the capsule is quite *robust* against a broad variation of the initial orientations with regards to ϕ_0 and θ_0.

---

[1] DOI M. and EDWARDS S. F., *The Theory of Polymer Dynamics* (Oxford University Press, Oxford) 1986.

[2] BRUNN P. O., *Int. J. Multiphase Flow*, **9** (1983) 187.

[3] DHONT J. K. G., *An Introduction to Dynamics of Colloids* (Elsevier, Amsterdam) 1996.

[4] SUCCI S., *The Lattice Boltzmann equation for fluid dynamics and beyond* (Clarendon Press, Oxford) 2001.

[5] DÜNWEG B. and LADD J. C. A., *Adv. Polym. Sci.* **221** (2009) 89.

[6] AIDUN C. K. and CLAUSEN J. R., *Annu. Rev. Fluid Mech.* **42** (2010) 439.

[7] ARNOLD A., LENZ O., KESSELHEIM S., WEEBER R., FAHRENBERGER F., ROEHM D., KOSOVAN P. and HOLM C., *ESPResSo 3.1 molecular dynamics software for coarse-grained models* (Springer, Berlin) 2013.

[8] LIMBACH H. J., ARNOLD A., MANN B. A. and HOLM C., *Comput. Phys. Commun.* **174** (2006) 704.

[9] KRÜGER T., VARNIK F. and RAABE D., *Computers and Mathematics with Applications* **61** (2011) 3485.

[10] KRÜGER T., *Computer simulation study of collective phenomena in dense suspensions of red blood cells under shear* (Universität Bochum, Bochum) 2011.

[11] HELFRICH W., *Zeitschrift für Naturforschung* **28c** (1973) 693.

[12] GUCKENHEIMER J. and HOMES P., *Nonlinear Oscillations, Dynamical Systems, and Bifurcations of Vector Fields* (Springer, Berlin) 1989.

[13] We remind that the mean orientation of the particle determines whether CSM exists or not in so far as $\langle\phi\rangle_T$ dictates in turn the location of the stiff and bendy contour part in regards to the upper and lower half-space, as discussed in the main text.